Coordination Chemistry Reviews 438 (2021) 213874

Contents lists available at ScienceDirect

Coordination Chemistry Reviews

journal homepage: www.elsevier.com/locate/ccr

Review

Materials Institute Lavoisier (MIL) based materials for photocatalytic applications

Suzhao Yang [a,b,1], Xin Li [a,b,1], Guangming Zeng [a,b,*], Min Cheng [a,b,*], Danlian Huang [a,b], Yang Liu [a,b], Chengyun Zhou [a,b], Weiping Xiong [a,b], Yang Yang [a,b], Wenjun Wang [a,b], Gaoxia Zhang [a,b]

[a] College of Environmental Science and Engineering, Hunan University, Changsha, Hunan 410082, China
[b] Key Laboratory of Environmental Biology and Pollution Control (Hunan University), Ministry of Education, Changsha, Hunan 410082, China

ARTICLE INFO

Article history:
Received 20 August 2020
Accepted 22 February 2021
Available online 22 March 2021

Keywords:
Photocatalysis
Metal-organic framework
Materials Institute Lavoisier

ABSTRACT

As one of the most effective method to convert solar energy into chemical energy, photocatalysis has gained extensive attention over the recent years. Attributes such as excellent porous structure, ultrahigh surface area and abundant active sites give Materials Institute Lavoisier (MIL) an edge over conventional photocatalyst. Furthermore, the structure, surface active sites, light response range and charge separation efficiency of MILs can be adjusted through reasonable design and modification. Herein, the research progress of MIL-based materials for photocatalytic applications is reviewed. Special attention is paid to the photocatalytic mechanism and primary strategies to improve the photocatalytic activity, including modification, doping and derivation, which are reviewed from the aspects of structure, optical properties, and stability. The synergistic effects between MILs and secondary components in MIL-based composites are compared and summarized. Additionally, the development opportunities and unsolved problems of MIL-based materials in the field of photocatalysis are also discussed.

Contents

* Corresponding authors at: College of Environmental Science and Engineering, Hunan University, Changsha, Hunan 410082, China.
E-mail addresses: zgming@hnu.edu.cn (G. Zeng), chengmin@hnu.edu.cn (M. Cheng).
[1] These authors contribute equally to this article.

https://doi.org/10.1016/j.ccr.2021.213874
0010-8545/

1. Introduction

The problem of energy depletion and environmental deterioration caused by the excessive use of fossil energy has always been a thorny one for human beings [1–8]. Therefore, the development of renewable clean energy is sought after by researchers [9,10]. Using infinite and sustainable solar energy to remove pollutants and produce energy is an effective and economical way to purify the environment and solve the energy shortage dilemma [11,12]. Photocatalysis, inspired by photosynthesis in green plants and microorganisms, has become a potentially green and co-effective technology to solve environmental and energy issue [13,14]. Since Fujisima and Honda took the lead in using TiO_2 as a photocatalyst to participate in the solar energy conversion process, the field of photocatalysis have made great progress [15]. A lot of photocatalytic researches are based on inorganic semiconductor materials, such as metal oxides [16,17], metal sulfides [18,19], etc. In recent years, new semiconductor graphitic carbon nitride (g-C_3N_4) has been widely studied [20,21]. However, due to the narrow optical response range, limited active sites and high charge recombination rate, the performance of traditional photocatalysts is not satisfactory [22]. Consequently, it is imperative to develop stable and high-performance light-responsive catalysts.

MIL (Materials Institute Lavoisier) materials are porous metal carboxylate salts composed of different trivalent metal cations and carboxylic acid ligands with huge pore and permanent porosity [23,24]. On the one side, MILs based on trivalent metal ions usually has high hydrothermal stability, which is very important for liquid phase catalysis [25–27]. On the other side, the main secondary building units (SBUs) caused by the trivalent cation and polycarboxylic acid can be formed under various conditions, indicating the rich synthesis paths of MILs [27]. In addition, an important advantage of MILs is that their micropore and mesopore structure can be changed under the stimulation of external factors, indicating the flexibility of the MILs structure [28]. As photocatalyst, MILs have unique and natural advantages, including: (1) As a multi-dimensional network with high order and periodicity, MILs have permanent and uniform pores and ultrahigh surface area, resulting in abundant active sites and excellent mass transfer capacity [29]. (2) The band structure of photocatalysts can be adjusted by modifying organic ligands or introducing functional substituents into organic ligands [30,31]. (3) The flexible frame structure allows other substrate materials to be loaded or encapsulated on the MILs, enabling surface or pores decoration of MILs [31]. (4) Some MILs with high stability and recyclability avoid complex and energy-consuming recycling procedures, resulting in a practical and sustainable MIL-based photocatalyst [32]. As far as we know, MIL-based materials work in the field of heterogeneous photocatalysis in two main aspects: (1) Pristine MILs as photocatalysts. The pristine MILs themselves can be employed in photocatalysis because of their catalytic metal sites, coordinative unsaturated metal ions, and active organic ligands [22]. As a solar energy converter, MILs can generate photogenic carriers after photo-excitation for subsequent redox reaction. Nevertheless, the wide band gap of the pristine MILs leads to poor solar energy utilization rate and low catalytic efficiency, thus resulting in unsatisfactory photocatalytic performance [33]. (2) Optimized MILs as photocatalysts. There are several strategies to optimize the photocatalytic activity of MILs, including modification [31], doping [34,35] and derivation [36]. Optimized MILs are indispensable in the area of photocatalysis because they can harvest light energy and/or transfer charge more efficiently, leading to the realization of the high performance of photocatalysts and the further development of MILs.

The past two decades have witnessed the flourish of MIL-based photocatalysts. The MIL-based materials have also been developed as photocatalysts for reduction of CO_2, splitting water, degradation of pollutants and organic transformation due to their effective charge separation efficiency and stability [37–39]. Actually, several papers provided comprehensive review on the synthesis and application of MOFs in photocatalysis [40,41]. For example, the team of Wang [33] reviewed the application of modified MOFs in environmental purification and disinfection under light exposure. Recently, Shi and co-workers [41] summarized the works of the mechanism and application of MOFs, MOFs composites and derived MOFs in splitting water. Additionally, some strategies to optimize the activity of MOF-based photocatalysts also have been summarized [42]. These rich works reflect the rapid development of MOF-based photocatalysts and great application potential. However, limited by the undefined bottlenecks of photocatalysis as well as the outdated and incomplete reports of MILs photocatalysts, a timely and systematic review is urgently needed. Herein, we systematically summarized the recent advances of MIL-based heterogeneous photocatalysts in environmental purification and energy production. MILs were divided into four categories, including pristine MILs, modified MILs, doped MILs and MIL-derived photocatalysts. Finally, the development prospects and future challenges of MILs in heterogeneous photocatalysis are proposed.

2. Pristine MILs photocatalysts

The organic ligands embedded in the MILs lattice can serve as active chromophores to absorb incident light, while metal nodes are considered to be isolated semiconductor quantum dots (QDs) that can be activated by light or organic ligands [43]. Therefore, pristine MILs can be directly used as photocatalysts to realize the light-induced reaction through charge transfer. Metal centers of MILs are the main active sites of photocatalysis, so the reasonable selection of metal clusters is of great significance to improve photocatalytic performance [42]. Some representative pristine MILs photocatalysts and their corresponding properties are listed in Table 1.

Table 1
Summary of pristine MILs for photocatalysis.

MIL	Structure/Morphology	Bandgap (eV)	Light source	Photocatalytic performance	Recycled times	Ref.
MIL-53(Fe)	Three-dimensional framework	2.72	Visible	60% Cr(VI) was reduced; 80% organic dye was degraded	4	[46]
MIL-88B(Fe)	Uniform spindle-like morphology	/	Visible	MB and RhB were degraded	3	[48]
MIL-68(Fe)	Three-dimensional framework	2.80	Visible	100% Cr(VI) was reduced	/	[49]
MIL-88A (H_2O_2)	Three-dimensional framework	/	Visible	MB was degraded	4	[29]
MIL-53(Fe) (H_2O_2)	/	/	Visible	100% RhB was degraded	3	[54]
MIL-53(Fe) (PS)	Rodlike structure	2.62	Visible	Almost 100% Acid Orange7 was degraded	5	[55]
MIL-88A(Fe) (PS)	Hexagonal microrods	2.25	Visible	TC was completely removed	5	[56]
MIL-125(Ti)	/	/	UV	Photooxidation of alcohols	/	[58]
MIL-167(Ti)	/	/	UV	The H_2 production rate reached 7.7 μmol h^{-1}	/	[59]
MIL-100(Ti)	/	3.40	UV	The H_2 production rate reached 1000 mmol g^{-1}	5	[57]
MIL-101(Cr)	Octahedron shape	/	UV	100% RBB was degraded	4	[61]
M−MILs (M = Fe, Al and Cr)	Well crystallized sphere-like particles	Fe 3.87, Al 3.20, Cr 2.72	UV–vis, visible	Almost no difference on the MB degradation	/	[62]

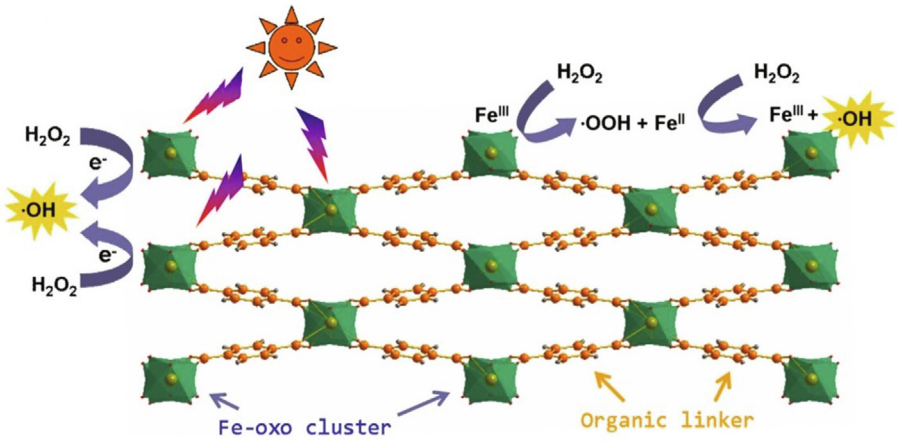

Fig. 1. Proposed mechanism for the activation of H_2O_2 by MIL-53(Fe) under visible light irradiation [54]. Copyright 2013 Elsevier.

2.1. Pristine Fe-based MILs photocatalysts

An outstanding advantage for Fe-based MILs is that they can be excited in visible light [44,45]. Representatively, MIL-53(Fe), an iron-containing porous crystal made of 1,4-benzenedicarboxylic acid linked to Fe(III) metal cluster, has been reported to be widely utilized for photocatalysis due to the visible light response of iron-oxo clusters [46,47]. In 2015, Liang and co-workers [46] used MIL-53(Fe) for photocatalytic removal of Cr(VI) and organic dyes simultaneously. The results suggested the rate of Cr(VI) reduction and organic dyes removal reached over 60% and 80%, respectively. Subsequently, Xu et al. [48] successfully synthesized the spindle-like MIL-88B(Fe) with uniform size. The results revealed that MIL-88B(Fe) showed a good photocatalytic degradation activity for methylene blue (MB) and rhodamine B (RhB) by using visible light. MIL-100(Fe) with the same metal clusters (Fe_3-μ_3-oxo) as MIL-88B(Fe) was also successfully prepared. In terms of visible-light catalytic activity, the former has a better performance [44]. Therefore, different organic ligands and topological structures with the same metal clusters will result in different photoactivity. In 2017, MIL-68(Fe) formed by the connection of terephthalic acid with $Fe(OH)_2O_4$ octahedron was prepared by solvent-thermal method for Cr(VI) reduction [49]. MIL-68(Fe) has been shown to respond to visible light and the Cr(VI) reduction rate reached 100% within 60 min.

Another interesting property of Fe-based MILs is that the presence of Fe(III) species enables them to combine photocatalytic techniques with advanced oxidation processes (AOPs) [40]. It is well known that the photocatalytic effect of MILs is realized through the participation of photogenerated electron (e^-) and hole (h^+) in the redox process [50]. In other words, photogenerated charge carriers play an indispensable role in photocatalytic reactions. Unfortunately, photogenerated electrons in MILs are easy to recombine with holes and reduce quantum yield [51]. When photocatalysis is combined with AOPs, photogenerated electrons in MILs can be consumed by oxidants (e.g., hydrogen peroxide, persulfate) in the advanced oxidation system, thus promoting charge separation [52,53]. For example, Xu and co-workers prepared MIL-88A(Fe) for MB degradation with the assistance of hydrogen peroxide (H_2O_2) [29]. In comparison to P25 TiO_2, the degradation rate of MB in MIL-88A(Fe)/Vis/H_2O_2 system gained a 2-fold enhancement. Based on the Fenton-like process, Fe-based MILs can be used as heterogeneous catalyst to decompose H_2O_2 into hydroxyl radicals (·OH), which decompose organic molecules by hydrogen extraction or hydrogenation [32]. The presence of H_2O_2 not only increases the source of active radicals but also promotes the effective separation of e^--h^+ pairs by consuming electrons [54]. As shown in Fig. 1, the iron-oxo clusters in MIL-53(Fe) are directly excited by visible light and then produce the e^- and h^+. The ferric species in Fe-MIL53 decompose H_2O_2 into ·OH by the

Fenton-like process (Eqs. (1) and (2)). In addition, ·OH can also be formed from H_2O_2 by capturing photo-induced electrons (Eqs. (3) and (4)). Consequently, the photocatalytic removal rate of RhB over MIL-53(Fe) was increased by 4.3 times with H_2O_2 served as electrons acceptor. This synergistic effect also exists in Fe-MIL/persulfate/Vis systems [55,56].

$$\text{Fe(III)species} + H_2O_2 \rightarrow \text{Fe(II)species} + HO_2\cdot + H^+ \quad (1)$$

$$\text{Fe(II)species} + H_2O_2 \rightarrow \text{Fe(III)species} + \cdot OH + OH^- \quad (2)$$

$$MIL-53(Fe) + hv \rightarrow h^+ + e^- \quad (3)$$

$$H_2O_2 + e^-(MIL-53(Fe)) \rightarrow \cdot OH + OH^- \quad (4)$$

2.2. Pristine Ti-based MILs photocatalysts

The electron transfer between Ti(III) and Ti(IV) in Ti-O cluster indicates the photoactivity of Ti-MILs [41]. One of the most important properties of Ti-MILs is their high thermal and chemical stability due to the high dissociation energy of O-Ti(IV) bonds [57]. Meenakshi et al. [58] first synthesized MIL-125(Ti) and demonstrated its robust thermal stability, high porosity, and photooxidation ability to alcohols. Hala et al. [59] isolated MIL-167, MIL-168, MIL-169, and "NTU-9-like" ("NTU-9-like" = $Ti(H_xDOBDC)_{1.5}(DEAH)_{2-1.5x}\cdot nsolv$)) crystalline phases from Ti(IV) precursor and 2,5-Dihydroxyterephthalic acid by solvent-thermal method, indicating the diversity of the system. MIL-167 with high microporosity had the highest hydrogen production rate under UV light. However, due to the higher reactivity and spontaneous hydrolysis of Ti precursors, the formation of titanium-oxocarboxylate clusters needs to be strictly controlled [57,60]. In view of this, Javier et al. [57] used a high-throughput approach to form classical SBUs that were not strictly controlled by the source of the metal. This method provides a feasible path for the controllable design of the new Ti-MOF structure. The SBUs are then linked by triacids to form MIL-100 topology, this MIL-100(Ti) inherits the chemical stability and mesoporosity inherent in the MIL-100 family. Based on ligand-to-metal charge transfer (LMCT) mechanism, MIL-100(Ti) can be used to produce hydrogen under UV light.

2.3. Pristine other metal-based MILs photocatalysts

Other metal-based MILs such as Al- and Cr-MILs also have optical activity. For example, the terephthalate ligands contained in the MIL-101(Cr) play a role of light-absorbing antennae and then transfer electrons to Cr_3O_{16} clusters. MIL-101(Cr) with large surface area (3360 $m^2\ g^{-1}$) and high crystallinity showed excellent performance in the process of photoinduced degradation of Remazol Black B (RBB) with UV as the source of light energy [61]. What's more, MIL-101(Cr) demonstrated to be superior stable that can be remained in the environment for several months [56]. In a previous study, Du et al. [62] demonstrated that the rates of light-induced MB removal of M−MILs (M = Fe, Al and Cr) have no difference. This result was striking because the Fe-MIL has the narrowest band gap and should have been more photoactive. The group of Yu [63] suggested that it is the metal nodes, not the organic linkers, that determine the type of photosensitization reactions. They demonstrated that Cr-MILs and Fe-MILs were subject to type I and II photosensitization, respectively, while Al-MILs showed poor photoactivity.

3. Modification of MILs photocatalyst

Although the development of novel MOFs provides a new option to improve their photocatalytic performance, most of the current studies still focus on the subtle modification of MOFs [64]. The ingenious modifications can alter MOFs features or introduce specific functionality that are not achievable with traditional synthesis methods [65]. Metal nodes and organic linkers are the two active sites of MILs, which can be functional modified to adjust the band structure or expose abundant active metal clusters. Some representative modified MILs photocatalysts and their corresponding properties are listed in Table 2.

3.1. On the basis of organic linkers

It is an effective method to extend the absorption of MIL-125 (Ti) to visible light region by using functional linker instead of or mixing with BDC linker. The addition of nitrogen atoms by adding amino groups to the organic ligand of MILs can not only narrow the band gap of photocatalyst but also effectively avoid crystal structure defects [64]. Based on this strategy, Fu and co-workers [66] obtained modified NH_2-MIL-125(Ti) using NH_2-1,4-benzenedicarboxylic acid (NH_2-BDC) as the linker and applied it to visible light-induced reduction of CO_2. Optimization of optical properties and enhancement of CO_2 absorption capacity enable NH_2-MIL-125(Ti) to reduce CO_2 under visible light. As can be seen from Fig. 2a, NH_2-MIL-125(Ti) shows an additional absorption band extending to 550 nm, demonstrating that NH_2-MIL-125(Ti) can be excited by visible light (400 nm < λ < 800 nm). This broadening of the absorbance range has been reported in other studies [67]. The strong electron-contributing property of aromatic functional groups causes the valence band to split into a high-energy occupied state, while the conduction band composed of O 2p and Ti 3d orbitals is not likely to be affected, resulting in the band gap reduction, and the light response range of the photocatalyst moves to the visible region. In addition to the optimization of optical properties, NH_2 group facilitated the interaction between CO_2 and functionalized aromatic groups of NH_2-MIL-125(Ti), thus enhancing the CO_2 absorption capacity of photocatalyst (see Fig. 2b) [66]. In NH_2-MIL-125(Ti)/Vis system, the yield of $HCOO^-$ reached 8.14 mmol within 10 h, while the control sample produced no $HCOO^-$ (see Fig. 2c). Although the photocatalytic rate is unsatisfactory, the potential of amino groups modified MIL-125(Ti) to reduction of CO_2 under visible light has been demonstrated. The mechanism of reduction of CO_2 in the NH_2-MIL-125(Ti)/Vis system is illustrated in Fig. 2d. Base on the mechanism of ligand-to-metal charge transfer (LMCT), the photoelectron in BDC-NH_2 transferred to Ti-O clusters to generate Ti(III), then CO_2 was reduced to HCOOH by Ti(III).

Different from NH_2-MIL-125(Ti), amino groups functionalized Fe-containing MILs have dual excitation routes, i.e., in addition to the excitation of functional organic likers, the iron-oxo clusters can be directly excited by visible light [45,68]. In a related study, the group of Wang [45] compared the CO_2 reduction rates of three types pure MILs (MIL-101(Fe), MIL-53(Fe) and MIL-88B(Fe)) and their corresponding amino groups functionalized iron-containing MILs. The photocatalytic properties of amine-functionalized MILs have been revealed to be significantly improved. The catalytic mechanism is shown in Fig. 3, the dual excitation path (the iron-oxo clusters and the organic linkers were excited simultaneously) led to the accumulation of large numbers of electrons on the iron-oxo clusters, and these electrons were transferred to Fe(III) through O_2^-, thus enabling CO_2 to be reduced by Fe(II). This series of amino functionalized MILs is subsequently used for photocatalytic reduction of CO_2 via the solvent-free reaction path. The selectivity of photocatalytic reduction of CO_2 to CO was significantly improved because of the higher contact probability between the photocatalyst and the reaction gas [69].

The effect of the incorporation of different functional groups (–NH_2, –OH, –CH_3, -Cl, -Br, -CF_3) on the optical response control

Table 2
Summary of modified MILs for photocatalysis.

MIL	Bandgap (eV)	Light source	Ligand	Photocatalytic performance	Recycled times	Ref.
NH_2-MIL-125(Ti)	/	Visible	$-NH_2$	Reduction of CO_2	/	[66]
NH_2-MIL-101(Fe) NH_2-MIL-53(Fe) NH_2-MIL-88B (Fe)	/	Visible	$-NH_2$	Amount of $HCOO^-$ reached to 178 μmol Amount of $HCOO^-$ reached to 46.5 μmol Amount of $HCOO^-$ reached to 30.0 μmol	/	[45]
NH_2-MIL-53(Fe) NH_2-MIL-88B(Fe) NH_2-MIL-101(Fe)	1.98 1.72 1.77	Visible	$-NH_2$	Photocatalytic reduction of CO_2 with superior selectivity to CO	4	[69]
MIL-125-X (X = $-NH_2$, –OH, $-CH_3$, -Cl, -Br, $-CF_3$)	MIL-125-CH_3/Cl 3.5 MIL-125-OH 2.8 MIL-125-NH_2 2.6	/	Various functional ligand	/	/	[70]
MIL-125-NH-X X = alkyl groups from methyl to heptyl	MIL-125-NH_2 2.56 MIL-125-NHMe 2.46 MIL-125-NHCy 2.29	Visible	Various functional ligand	The rate of photoreduction of CO_2 increased with the increase of the number of carbon atoms in the N alkyl chain	/	[71]
MIL-125(Ti)-AM-Eu	/	UV	-AM-Eu	/	5	[74]
Cu-NH_2-MIL-125(Ti)	/	Visible	/	The H_2 production rate reached 490 mmol$g^{-1}h^{-1}$	/	[75]
Fe/NH_2-MIL-68(In)	NH_2-MIL-68 (In) 2.91	Visible	/	99.29% Cr(VI) was removed	3	[77]
Fe/NH_2-MIL-125(Ti)	1.83	Visible	/	Nearly 100% of Orange II was removed within10 min	4	[78]
NH_2-MIL-125(Ti)	/	Visible	(1 1 0) facet	The H_2 production rate reached 60.8 mmol $g^{-1}h^{-1}$	3	[82]

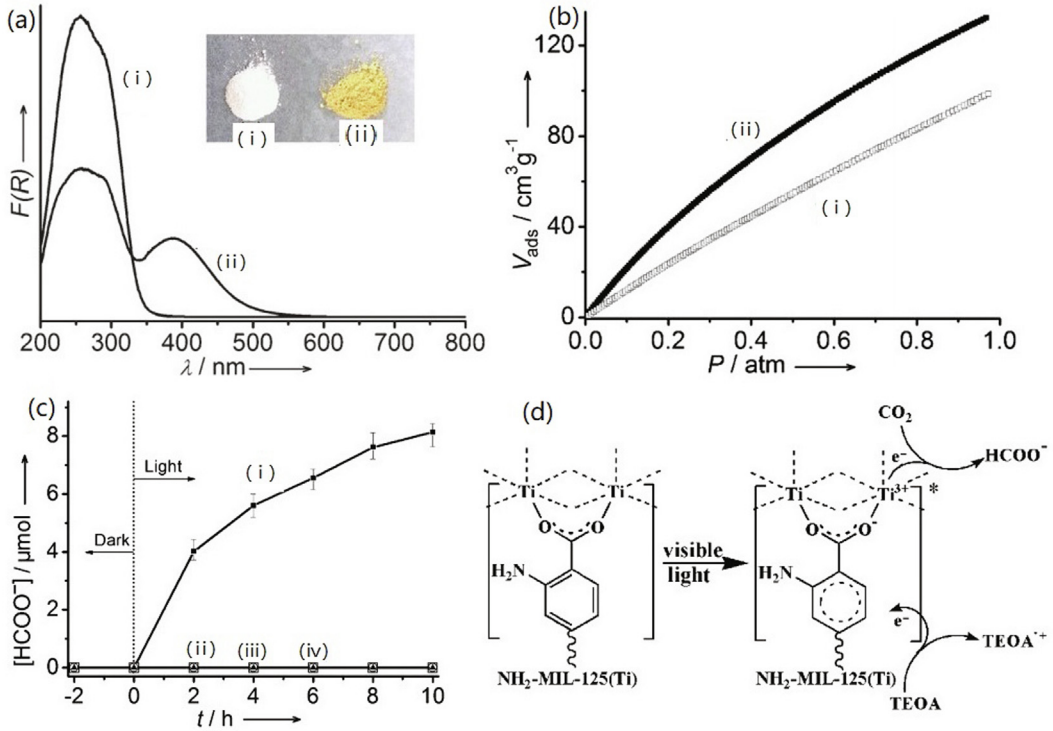

Fig. 2. (a) UV/vis spectra of (i) MIL-125(Ti) and (ii) NH_2-MIL-125(Ti); (b) CO_2 adsorption isotherms (1 atm, 273 K) of (i) MIL-125(Ti) (□) and (ii) NH_2-MIL-125(Ti) (■); (c) the amount of $HCOO^-$ produced as a function of the time of irradiation over (i) NH_2-MIL-125(Ti) (■), (ii) MIL-125(Ti) (□), (iii) a mixture of TiO_2 and H_2ATA (19 mg + 32 mg) (○) and (iv) visible light irradiation without a sample (▲); (d) proposed mechanism for the photocatalytic CO_2 reduction over NH_2-MIL-125(Ti) under visible light irradiation [66]. Copyright 2012 Wiley-VCH.

ability of modified MIL-125(Ti) was revealed by Hendon et al. [70]. The $-CF_3$ group as a strong electron-withdrawing group only slightly reduced the band gap and led to instability of the Ti-O bond. Other groups ($-NH_2$, –OH, $-CH_3$, -Cl) decreased the band gap to varying degrees and demonstrated to be promising substituent. Moreover, the binary aminated BDC-$(NH_2)_2$ linker showed the maximum redshift, with 10%-MIL-125-$(NH_2)_2$/90%-MIL-125-NH_2 forming a 1.3 eV optical band gap and the absorption region extended to 950 nm. However, this result does not mean that the higher the doping ratio of amino groups is, the better the performance of MIL-based photocatalysis is. The group of Caroline confirmed that the catalytic performance of modified MIL-125(Ti) reached equilibrium when the doping ratio of amino groups was about 50% [66]. They speculate that the intrinsic properties of solid composites are responsible for this equilibrium. The Ti^{3+}-Ti^{4+} pairs were formed via electron transfer after photoexcitation of NH_2-

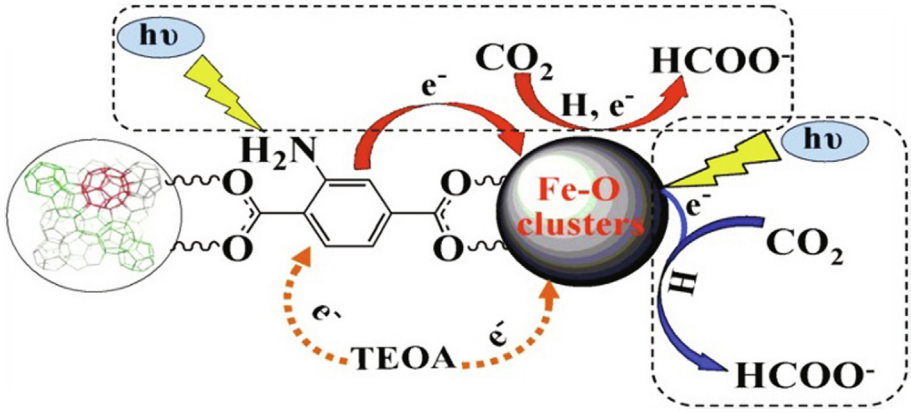

Fig. 3. Dual Excitation Pathways over Amino-Functionalized Fe-Based MOFs [45]. Copyright 2014 American Chemical Society.

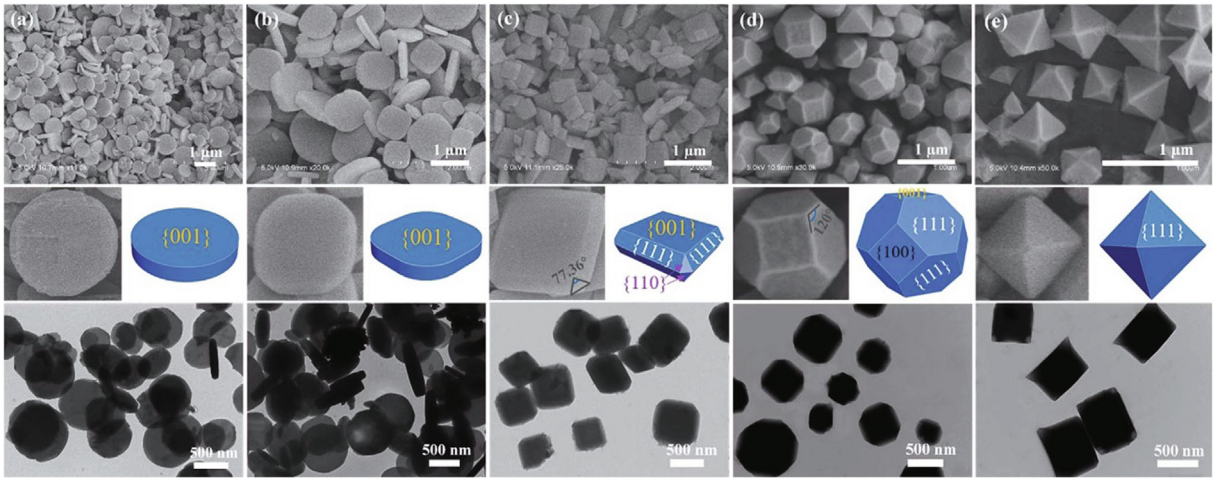

Fig. 4. SEM, enlarged SEM, TEM images and the corresponding 3D geometry models of as-synthesized NH2-MIL-125(Ti) [82]. Copyright 2019 The Royal Society of Chemistry.

MIL-125(Ti) and then participated in the following redox reaction. However, the excess Ti^{3+}-Ti^{4+} pairs with the Ti_8-wheel structure result in the imposition of electrostatic penalty, thus prevents the additional NH_2-BDC from producing catalytic center. Recently, Logan et al. [71] prepared various isologue of MIL-125-NH2 whose amino groups were modified by alkyl groups with increasing chain length and varying connectivity. The introduction of functional groups resulted in the decrease in band gap from 2.46 eV for MIL-125-NHMe (Me = methyl) to 2.29 eV for MIL-125-NHCyp (Cyp = cyclopentyl). MIL-125-NHCyp with a small bandgap, a long-lived excited-state (τs = 68.8 ns) and the high apparent quantum yield (Φ_{app} = 1.80%), showed a better photocatalytic efficiency than the parent MIL-125-NH_2 (E_g = 2.56 eV, Φ_{app} = 0.31%, τs = 12.8 ns). In addition, other functional groups such as $-NO_2$, -Br [72] and $-SCH_3$ [73] are also used to enhance the visible light response of MILs.

Apart from the doping of these nonmetallic atoms, strategies to optimize the performance of MIL-based photocatalyst by modifying $-NH_2$ containing linker with metal ions have also been gradually developed. For example, MIL-125(Ti)-amide-europium (MIL-125(Ti)-AM-Eu) was synthesized via covalent postsynthetic modification [74]. MIL-125(Ti)-amide can provide sufficient binding sites for the incorporation of lanthanide metal ions. The introduced europium ions (Eu^{3+}) can create an antenna effect with pyridine in MIL-125(Ti)-AM, thus enhancing the luminescence effect of Eu^{3+}. The MIL-125(Ti)-AM-Eu was demonstrated to selectively oxidize α-phenethyl alcohol under UV irradiation. More recently, non-noble metal Cu^{2+}/Cu^{+} was attached to the linkers of NH_2-MIL-125(Ti) to form mixed valence redox centers [75]. The charge density and lifetime of photogenerated charges of copper-modified NH_2-MIL-125(Ti) (Cu-NM) boosted by 7000 times and 27 times respectively. Consequently, the photocatalytic hydrogen production rate of Cu-NM reached 490 mmol $g^{-1}h^{-1}$, which is 27 and 10 times than that of NH_2-MIL-125(Ti) and Pt-NH_2-MIL-125(Ti), respectively.

3.2. On the basis of metal notes

The metal nodes of MOFs are coordinated with the solvent molecules (e.g., N, N-Dimethylformamide, H_2O), which can be removed by heating or vacuum activation to generate coordinatively unsaturated metal sites (CUSs), thus enabling MOFs to participate in the Lewis acid catalytic reaction [65]. However, these metal nodes are often blocked by organic ligands, which results in low activity [31]. Therefore, the modification of metal nodes to provide more effective active sites is an effective means to improve the photocatalytic performance of MILs. Zhang et al. [76] revealed that Ru partially replaces Ti in MIL-125-NH_2, leading to more Ti-O clusters being exposed. Similar result was also reported by Wang et al [77]. They successfully synthesized $In_\alpha Fe_{1-\alpha}$ based MOFs NH_2-MIL-68 and demonstrated that the size of Fe(III) was smaller than In(III), which caused the pore volume to be somewhat enlarged and exposed more active sites. Similarly, bimetallic Fe/

Table 3
Summary of doped MILs for photocatalysis.

MIL	Structure/Morphology	Bandgap (eV)	Light source	Photocatalytic performance	Mechanism	Recycled times	Ref.
Pt/MIL-125(Ti)–NH_2	Pt NPs deposited onto MIL-125(Ti)–NH_2	/	Visible	The H_2 production rate reached 5.17 μmol h^{-1}	e^-	3	[84]
Pt/MIL-100(Fe)	Pt deposited on the surface of MIL-100(Fe)	/	Visible	The maximum rate of H_2 production reached 109 μmol $g^{-1}h^{-1}$	e^-	3	[85]
MIL-125-CoPi-Pt	Pt and CoPi co-deposited onto MIL-125(Ti)	/	UV–Vis	The evolution rates of H_2 and O_2 were 42.33 and 21.33 μL h^{-1} respectively	e^-, h^+	/	[86]
Pd@MIL-100(Fe)	Pd NPs dispersed on the surface of MIL-100(Fe)	/	Visible	Three typical PPCPs was degraded	e^-, ·OH	4	[87]
(Au, Pd, and Pt) NPs on the MIL-100(Fe)	(Au, Pd, and Pt) NPsdispersed over MIL-100 (Fe)	/	Visible	Pt@MIL-100(Fe) > Pd@MIL-100 (Fe) > Au@MIL-100(Fe) > MIL-100(Fe)	e^-, ·OH	4	[88]
Pd@MIL-100(Fe)	Pd NPs immobilized into the pores of MIL-100(Fe)	/	Visible	Pd@MIL-100(Fe) > Pd/MIL-100(Fe)	/	5	[89]
Pd/MIL-101(Fe)–NH_2	Pd supported on MIL-101 (Fe)–NH_2	/	Visible	77% benzyl alcohol was produced with a full benzaldehyde conversion	/	5	[90]
MIL-101(Cr)-Ag	Ag supported on MIL-101 (Cr)	/	Visible	CO, CH_4, and H_2 production rates were 808.2, 427.5, and 82.1 μmol $g^{-1}h^{-1}$	/	/	[92]
M/Ti-MOFs (M = Pt and Au, Ti-MOFs = MIL-125-NH_2 and MIL-125)	(Pt, Au) NPs highly dispersed on surface of MOFs	Pt/MIL 2.2 Au/MIL 2.38	UV–Vis	Pt/MIL-125-H_2 > Au/MIL-125-NH_2 > MIL-125-NH_2	e^-, $.O_2^-$	4	[93]
Pt@MIL-125/Au	Core-shell heterostructure	3.72	Visible	The H_2 production rate reached 1743.0 μmol $g^{-1}h^{-1}$	e^-	3	[94]
Co@MOF	Core-shell structure	/	Visible	The H_2 evolution efficiency of Co@MOF was 20 folds that of NH_2-MIL-125(Ti)	e^-	3	[95]
Co(II)@MOF	Core-shell structure	/	Visible	The H_2 production rate reached 553 μmol $g^{-1}h^{-1}$	e^-	3	[96]
Ni@NH_2-MIL-125(Ti)	Globular structure with an internal layered morphology	/	UV	The composite demonstrated a TOF of 28 mol H_2 $g_{(Ni)}^{-1}h^{-1}$	/	/	[97]
MIL-101(Cr)/Ni(dmgH)$_2$	/	/	Visible	The H_2 production rate reached 45.5 mmol h^{-1}	e^-	/	[98]
NiMo@MIL-101	NiMo nanocluster anchored on MIL-101	/	Visible	The H_2 production rate reached 740.2 μmol·h^{-1}	e^-	4	[99]
CoPOM/MIL-100(Fe)	/	/	Visible	The O_2 production rate reached to 7.5 mmol h^{-1} g^{-1}	/	/	[101]
CoPOM/MIL-101(Cr)	CoPOM dispersed inthe channel of MIL-101	/	Visible	The O_2 production rate reached to 6.7 mmol h^{-1} g^{-1}	/	/	[102]
NH_2-MIL-125/TiO_2	TiO_2 (P25) particles were dispersed on the surface of NH_2-M125	2.70	Visible	Selective oxidation of cyclohexane	h^+, e^-, $.O_2^-$, and ·OH	4	[110]
MIL-100(Fe)/TiO_2	/	3.03	UV	85.8% TC was degraded50% Cr(VI) was reduced	h^+, .OH and O_2^- (TC) e^- (Cr(VI))	/	[111]
TiO_2@MIL-101	Double-shell hollow structure	2.89	UV	90.1% H_2S was converted	.OH, H_2O_2	/	[112]
TiO_2@NH_2-MIL-88B(Fe)	Catkin-shaped TiO_2 was attached to the surface of Fe-MOF	2.16	Visible	100% MB was degraded	.OH	5	[113]
TiO_2NS@MIL-100(Fe)	Hierarchical heterostructures	/	Visible	TiO_2NS@MIL-100(Fe) displayed the highest rate constant (0.045 min^{-1}) for MB degradation	h^+, .OH	4	[114]
Fe_3O_4@MIL-100(Fe)	Core-shell microspheres structures	/	UV–vis	99% MB was removed	h^+, .OH	5	[117]
MIL-100(Fe)@Fe_3O_4/CA	/	1.76	Visible	85% TC was degraded	·OH, $.O_2^-$	7	[115]
Fe_3O_4/MIL-88B(Fe)	Hierarchical nanoarchitectures	1.89	Visible	99.8% RhB was degraded	h^+, .OH	4	[118]
CdS/MIL-100(Fe)	CdS NPs were attached on the surface of MIL-100(Fe)	2.23	Visible	Selective oxidation of benzyl alcohol to benzaldehyde	h^+, $.O_2^-$	5	[123]
Au@CdS/MIL-101	Heterojunctions	/	Visible	The H_2 production rate reached 250 mol h^{-1}/ 10 mg	e^-	/	[129]
CdS QDs@MIL-101	Core-shell structure	/	Visible	Synthesis of imines with high selectivity	/	4	[127]
CdS QDs /NH_2-MIL-125@TiO_2	Core-shell structure	/	Visible	Oxidation of NO	.OH, $.O_2^-$	/	[131]
In_2S_3@MIL-125(Ti)	Core-shell structure	2.28	Visible	63.3% TC was degraded	·OH, $.O_2^-$	3	[133]
NH_2-MIL-125(Ti)@$ZnIn_2S_4$/CdS	layered tandem heterojunction	1.84	UV–vis	The H_2 production rate reached 2.367 mmol $g^{-1}h^{-1}$	e^-	5	[134]
1T-MoS_2/MIL-125-NH_2	1T-MoS_2 attached on and cover the surface of MIL-125-NH_2	/	Visible	The H_2 production rate reached 1454 μmol h^{-1} g^{-1}	e^-	6	[137]
1TMoS_2@MIL-53(Fe)	/	/	Visible	Ibuprofen was degraded with 95% neralization efficiency	.OH, $.O_2^-$, e^-	5	[138]
BiOBr/NH_2-MIL-125(Ti)	2D lamellar structure	2.70	Visible	80% of RhB was degraded for 100 min	h^+, $.O_2^-$	4	[142]

(*continued on next page*)

Table 3 (*continued*)

MIL	Structure/Morphology	Bandgap (eV)	Light source	Photocatalytic performance	Mechanism	Recycled times	Ref.
BiOI/MIL-88B(Fe)	3D hierarchical structure	/	UV–vis	88% of RhB was degraded for 100 min	h^+, .OH	5	[140]
Ag_3PO_4@ NH_2-MIL-125	Core-shell structure	2.39	Visible	Compared with P25, the photoactivity of MB and RhB increased by 39 times and 35 times, respectively.	h^+, $.O_2^-$	5	[143]
Ag_2WO_4@ NH_2-MIL-125	Core-shell structure	2.27	VisibleUV	/	$.O_2^-$, .OH	5	[144]
GR/MIL-53(Fe)	Two-dimensional nanosheet	2.72	Visible	20 mg/L RhB was degraded within 60 min	/	/	[148]
MIL-53(Fe)-rGO	/	2.72	Visible	100% Cr(VI) was removed for 80 min	e^-	/	[149]
MIL-88(Fe)@GO	Layered-structure	/	UV–vis	100% MB and RhB were degraded at 20 and 30 min, respectively	/	/	[154]
NH_2-MIL-53(Al)/rGO	Hollow microsphere structure	2.40	Visible	The efficiency of photodegradation of MB was improved	/	3	[155]
g-C_3N_4/MIL-125(Ti)	Heterostructure	3.24	Visible	The photodegradation rate for RhB was 0.0624 min^{-1}	h^+, $.O_2^-$	5	[162]
g-C_3N_4/MIL-101(Fe)	Heterostructure	2.75	Visible	Nearly 98% bisphenol A was degraded for 60 min	h^+, $.O_2^-$, SO_4^-	5	[163]
NH_2 MIL-101(Fe)/g C_3N_4	Heterostructure	/	Visible	The highest CO production rate reached 132.8 μmol g^{-1}	e^-	6	[164]
g-C_3N_4-MIL-53(Fe)	Blocky structure	/	Sunlight	The H_2 production rate reached 0.9054 mmol $g^{-1}h^{-1}$	e^-	3	[165]
MIL-125(Ti)/Pt/g-C_3N_4	Hierarchically meso- and microporous structure	/	Visible	The H_2 production rate reached 3986 μmol h^{-1} g^{-1}	e^-	/	[167]
NH_2-MIL-125(Ti)/CN/NiPd	Heterostructure	/	Visible	The H_2 production rate reached 8.7 mmol $g^{-1}h^{-1}$	e^-	4	[168]
g-C_3N_4/PDI@ NH_2-MIL-53 (Fe)	Heterostructure	2.15	Visible	Several water-soluble and toxic organic pollutants were removed	.OH	5	[169]
CFB/NH_2-MIL-125(Ti)	Z-Scheme heterostructure	/	Visible	The H_2 production rate reached 1.123 mmol h^{-1} g^{-1}	e^-	/	[170]
MIL-88A/g-C_3N_4	Z-scheme heterostructure	/	Visible	100% RhB was degraded for 30 min	h^+, $.O_2^-$, .OH	/	[171]
NH_2-MIL-88B(Fe)/CDs	/	1.98	Visible	Cr(VI) was reduced completely	e^-	4	[173]
SiO_2/MIL-100(Fe)	Core-shell structure	/	Visible	94% RhB was removed within 90 min	h^+, .OH	3	[176]

NH_2-MIL-125(Ti) has been successfully synthesized and proved to be an effective solar photocatalyst due to the narrow band gap [78]. Moreover, the presence of iron sites can activate persulfate (PS). Consequently, almost 100% Orange II was degraded within 10 min in the Fe/Ti-MOFs-NH_2/PS/Vis system.

Another way to expose more active metal centers is to perform facet engineering on MILs. This strategy is very common in improving the surface activity of traditional nanocatalysts, but its application to soft crystal MOFs is rarely reported [79–81]. Recently, Guo et al. [82] controlled the facets of nanostructured NH_2-MIL-125(Ti) by altering the concentration of the structure-capping surfactant cetyltrimethylammonium bromide (CTAB) (see Fig. 4). The presence of more metal clusters on the plane leads to more active photoactivity. Therefore, the NH_2-MIL-125(Ti) with active (1 1 0) facet showed a higher quantum yield, and the photocatalytic hydrogen production rate was three times higher than that of the sample with a dominant (1 1 1) facet.

4. Doping of MILs photocatalyst

Despite the outstanding photocatalytic performance of MILs, the active center of the original MILs was only limited to metal nodes and organic ligands, leading to limited reactivity. The flexible structure of the MILs allows them to host guest components, thus resulting rich active sites and synergistic effects [65]. Some representative doped MILs photocatalysts and their corresponding properties are listed in Table 3.

4.1. On the basis of metal

4.1.1. Metal nanoparticles

Prolonging photogenerated charge life and ensuring e^--h^+ pair separation are the key factors to boost photocatalytic efficiency, which can be achieved through the synergistic catalysis of MILs and metal nanoparticles (NPs) [50]. The highly ordered multi-dimensional network and adjustable frame structure of MILs make it possible for metal NPs to be evenly distributed on the surface or encapsulated in the cavities of MILs [83]. Interestingly, the role of different metal NPs in photocatalytic processes may vary greatly.

Pt metal particles are the most common and efficient co-catalyst for photocatalytic hydrogen production. Yu et al. [84] successfully fabricated Pt/MIL-125(Ti)–NH_2 in 2012, which demonstrated the high efficiency for photocatalytic H_2 production due to the efficient charge separation. However, the Pt/MIL-125(Ti)–NH_2 suffered from structural collapse and Pt NPs leaching during the photocatalytic process. In order to obtain more stable photocatalyst, Wang et al. [85] deposited Pt on a water stable Fe-containing MOF (MIL-100(Fe) by one-step photoreduction. Moreover, Pt/MIL-100(Fe) exhibited boosted performance for H_2 evolutionary as compared to Pt/MIL-100(Fe)-$NaBH_4$, which Pt NPs were obtained through $NaBH_4$ reduction. This difference is attributed to the fact that photoreduction is a mild process, making it easier to form Pt NPs with uniform size. In a further study, the simultaneous production of H_2 and O_2 from the overall water splitting was achieved by co-deposition Pt and CoPi alloy on MIL-125(Ti) [86]. Pt and CoPi can reduce the overpotential of hydrogen- and oxygen-producing reactions thus achieving efficient water decomposition. In addition, photoexcited electrons transferred to Pt NPs, while h^+ moved to CoPi, so that the e^- and h^+ can be separated effectively.

Pd particles with high Fermi energy levels can also optimize the photocatalytic performance of MILs through the synergistic catalysis. In 2015, Liang's team [87] prepared Pd@MIL-100(Fe) by alcohol reduction with H_2PdCl_4 as Pd precursor. Due to the excellent photoactivity and effective inhibition of photoinduced carrier recombination, the photocatalytic rate of Pd@MIL-100 (Fe) was significantly higher than that of Pd@$TiO_{2-x}N_x$ and Pd@Fe_2O_3 [87]. The results of quenching experiments showed that e^- and ·OH

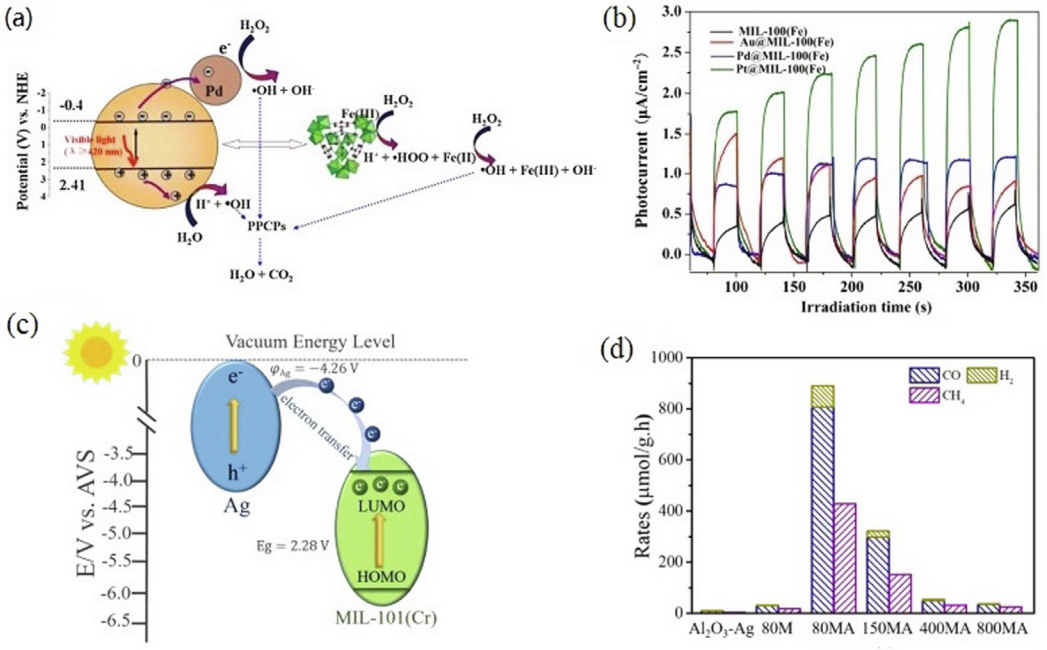

Fig. 5. (a) Proposed mechanism for the photocatalytic degradation of PPCPs over Pd@MIL-100(Fe) [87]. Copyright 2015 Elsevier. (b) Transient photocurrent response of MIL-100(Fe) and M@MIL-100(Fe) (M = Au, Pd, and Pt) under visible-light irradiation ($\lambda \geq 420$ nm) [88]. Copyright 2015 Spring. (c) Schematic Illustration of the Electron Transfer Process in MIL-101(Cr)-Ag Hybrids. (d) photocatalytic CO_2 reduction performances for varied catalysts [92]. Copyright 2019 American Chemical Society.

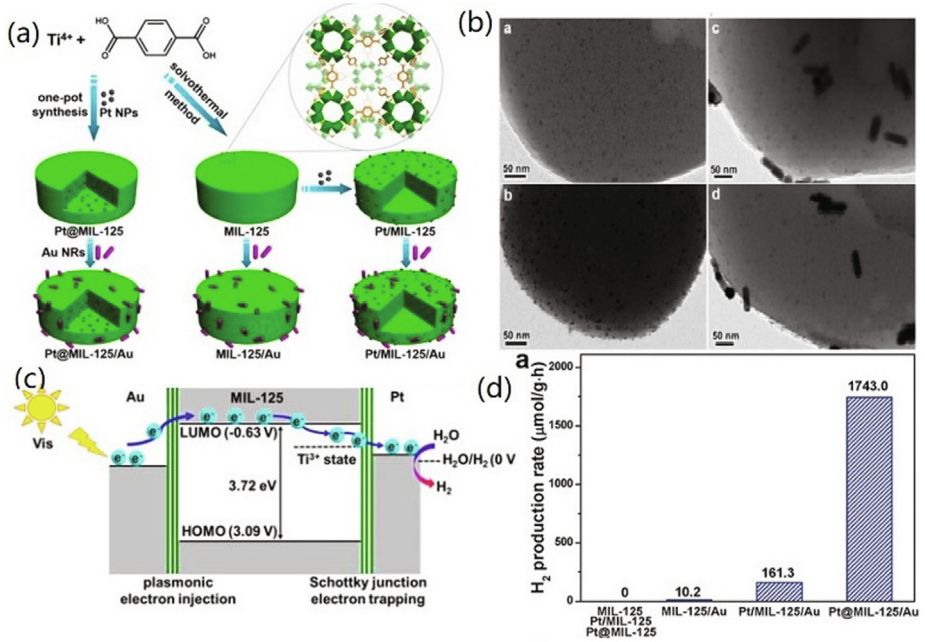

Fig. 6. (a) Schematic illustration showing the rational synthesis of photocatalysts. (b)Typical TEM images. (c) Comparison of the photocatalytic H_2 production rates of different catalysts. (d) Schematic illustration showing the electron migration at the two metal-MOF interfaces [94]. Copyright 2017 Wiley-VCH.

played important roles during photocatalysis process. There are three pathways to generate ·OH as shown in Fig. 5a: (1) H_2O was trapped by the h^+ and formed **.**OH; (2) H_2O_2 acted as a scavenger to capture e^- from Pd NPs to generate ·OH; (3) The ferric species on Pd@MIL-100 (Fe) decomposed H_2O_2 into **.**OH through the Fenton-like process. Additionally, this research team also prepared M@MIL-100(Fe) (M = Au, Pd, Pt) through room-temperature photodeposition process to compare the photoactivity of MIL-based complex doped with different metal NPs [88]. As shown in Fig. 5b, the photocurrent transient response revealed the photocurrent density of Pt@MIL-100 (Fe) was highest compare to Pd@MIL-100 (Fe) and Au@MIL-100 (Fe), revealing the most effective photocarriers separation of Pt@MIL-100(Fe). Pt NPs have a smaller particle size than Au NPs and Pd NPs, so the electron transfer efficiency on Pt@MIL-100(Fe) was higher. In addition, the spatial structure of Pd/MILs also affects the photocatalytic efficiency. Wang et al. [89] demonstrated that Pd@MIL-100(Fe) composed of Pd precursors dispersed in MIL-100(Fe) pores was more

stable and active than the Pd/MIL-100(Fe), which immobilized Pd NPs to the outer surface of MIL-100(Fe). The photocatalytic results showed that Pt@MIL-100(Fe) had a better performance in degrading methyl orange (MO) and reducing Cr(VI). Small size Pd NPs encapsulated in cavity of MIL-100(Fe) not only provide more abundant active sites, but also shorten the distance between Fe-O clusters and Pd NPs to achieve rapid electron transfer. Specially, the fixing effect of Pd NPs can be enhanced by amino groups of MIL-101(Fe)–NH_2 [90]. The density functional theory (DFT) calculation revealed strong interaction between Pd NPs and –NH_2, indicating the stabilization of amino group, which enables Pd NPs to be evenly and highly dispersed on the surface of MIL-101(Fe)–NH_2. The electron density of Pd center also increased with the incorporation of –NH_2.

The surface plasmon resonance characteristics of Ag and Au promote the generation of hot electrons under visible light and inject them into the CB of MILs, effectively improving the solar energy utilization [64,91]. Guo et al. [92] demonstrated the potential of MIL-101(Cr)-Ag in energy production. They demonstrated that the absorption spectrum of MIL-101(Cr)-Ag hybrids was widened to the visible range, and the surface defect state of Ag center was reduced after being deposited on MIL-101(Cr). Therefore, charge recombination was effectively prevented in the complex, thus achieving an increase in CO_2 reduction efficiency driven by visible light. Unlike Pd NPs as an electron trap in Pd@MIL-100 (Fe) [87], Ag NPs in MIL-101(Cr)-Ag can be excited by visible light to generate e^--h^+ pairs, and then photogenerated electrons are transferred to MIL-101(Cr) (see Fig. 5c). The smaller MIL-101(Cr) with higher density of edge and corner sites can capture more photons. As shown in Fig. 5d, 80MA (MIL-101(Cr)-Ag with 80 nm MOF) achieved the highest performance of photocatalytic CO_2 reduction, and the yields of CO, CH_4, and H_2 were 808.2, 427.5, and 82.1 μmol $g^{-1}h^{-1}$.

Similarly, Au-doped Ti-MIL showed improved photocatalytic performance, but had different modification effects compared with Pt-doped Ti-MIL. In comparison to pure Ti-based MILs and Au/Ti-MILs, the catalytic rate of Pt/Ti-MILs was increased by 2.4 times and 1.9 times, respectively [93]. On the basis of the above research, the plasmonic effect and Schottky junction were integrated into MIL-125(Ti) by constructing two metal-MOF interfaces (Pt-MIL and Au-MIL) [94]. As shown in Fig. 6a,b, Pt/MIL and Pt@MIL were obtained by dispersing Pt NPs over or into MIL-125(Ti). Subsequently, Au nanorods were fixed on Pt@MIL, Pt/MIL and the pristine MIL to prepare Pt@MIL-125/Au, Pt/MIL-125/Au and MIL-125/Au. Pt NPs act as electrons acceptors and form Schottky structures, while Au nanorods possess surface plasmon resonance that respond to visible light. The photocarrier transport in the composite was controlled from three aspects (see Fig. 6c): (1) Plasma electrons excited by visible light on the surface of Au NPs were injected into MIL-125(Ti), and Ti^{4+} was reduced to Ti^{3+}; (2) The electrons were transferred to Pt NPs induced by Schottky barrier; (3) The electrons on the surface of Pt NPs were rapidly consumed due to the exquisite structural design of the catalyst. The relative spatial position of metal NPs and MIL-125 also affects the photocatalytic efficiency. Consequently, the Pt@MIL-125/Au presented the best efficiency for visible light induced H_2 production (see Fig. 6d).

4.1.2. Metal complexes

Some studies avoided the use of noble metals and effectively enhanced the performance of photocatalysts through host–guest strategy. In 2015, Nasalevich and co-workers [95] encapsulated Co-dioxime-diimine into NH_2-MIL-125(Ti) by two-stage "ship-in-the-bottle" approach (see Fig. 7). The results showed that H_2 production efficiency of Co@MOF was 20-fold higher than that of pure NH_2-MIL-125(Ti). Similarly, Jiang et al. [96] immobilized [Co^{II}(TPA)Cl][Cl] (TPA = tris(2-pyridylmethyl)-amine) into the cages of MIL-125-NH_2 to obtain Co(II)@MOF for light-driven H_2 production. As a co-catalyst and active center, encapsulated Co(II) complex not only regulated the energy level of CB/LUMO, but also accumulated electrons for reducing protons to H_2. Consequently, the Co(II)@MIL-125-NH_2 outperformed pure MIL-125-NH_2, Co complexes and their physical mixtures in terms of H_2 evolution. Moreover, Co species were encapsulated in the MOF caves to achieve the heterogeneity and thus prevent Co leaching. Therefore, the Co(II)@MIL-125-NH_2 showed remarkable reusability during photocatalytic water splitting.

In 2016, Meyer and co-workers [97] introduced the nickel(II) catalyst [Ni(dmobpy)(2-mpy)$_2$] (dmobpy = 4,4′-dimethoxy-2,2′-bipyridine, 2-mpy = 2-mercaptopyridyl) with high proton reduction activity into NH_2-MIL-125(Ti) and successfully assembled the Ni@NH_2-MIL-125(Ti), which is the first MIL-based photocatalyst containing Nickel(II) species. In Ni@NH_2-MIL-125(Ti)/light system, the H_2 yield was 1800 times than that of bare NH_2-MIL-125 (Ti) and one order of magnitude higher than [Ni(dmobpy)(2-mpy)$_2$] molecular catalyst. Furthermore, the catalytic activity of Ni@NH_2-MIL-125(Ti) was increased tenfold and was prolonged for 3000 min. Subsequently, the MIL-101(Cr)/Ni(dmgH)$_2$ hybrid was obtained via loading Ni(dmgH)$_2$ onto MIL-101(Cr) by Wang and co-workers [98]. With the assistance of sacrificial agent triethanolamine (TEOA) and the photosensitization of Erythrosin B, the photocatalytic efficiency of MIL-101(Cr)/Ni(dmgH)$_2$ gained a 10-fold increase compared to the pure MIL-101(Cr). In a further work, Zhen and co-workers [99] successful synthesized NiMo@MIL-101 through a double solvents method for photocatalytic H_2 production with Eosin Y (EY) as photosensitizer. EY was stimulated by light to produce EY1* and then formed EY3*. Subsequently, EY3* reacted with TEOA to produce EY^-, then e^- was transferred to $MoNi_4$ active site, and finally H^+ captured e^- from $MoNi_4$ to produce H_2. The catalyst can be well recycled owing to the unique shell-core structure.

4.1.3. Polyoxometalates (POMs)

POMs, a metal–oxygen cluster consisting of transition metals and oxygen atoms, play an important role in the catalytic process because of its stable structure and high activity [41]. Incorporating the POMs into the MILs as part of framework of MILs or encapsulated into cavity of MILs is a promising strategy to modify MIL-based materials, which not only enhances the structural stability of MILs but also combines the advantages of POMs and MILs [100]. Shah et al. and Han et al. [101,102] constructed heterogeneous catalysts with good recyclability by encapsulating Co-based POM ($[Co_4(PW_9O_{34})_2(H_2O)_2]^{10-}$) in the cavities of MIL-100 (Fe) and MIL-101(Cr), respectively. In both cases, the performance of photocatalytic O_2 production by splitting water was improved, and the high O_2 yield of CoPOM/MIL can be attributed to the favorable interaction between host (MIL) and guest (Co-based POM). However, the O_2 production rate and turnover frequencies of CoPOM/MIL-101(Cr) (66%; 7.3×10^{-3} s^{-1}) were lower than that of CoPOM/MIL-100(Fe) (72%; 9.2×10^{-3} s^{-1}) because the MIL-101(Cr) framework with large window size leads to easy leaching of CoPOM thus resulting in reduced photocatalytic activity.

4.2. On the basis of metal semiconductor

Considering the high cost and complex synthesis of metal NPs, the application of metal loaded MILs is limited to some extent. The close-contact heterojunction formed by metal semiconductor and MILs can accelerate charge transfer effectively [64]. Therefore, metal–semiconductor doped MILs can be used as an alternative to improve photocatalytic performance.

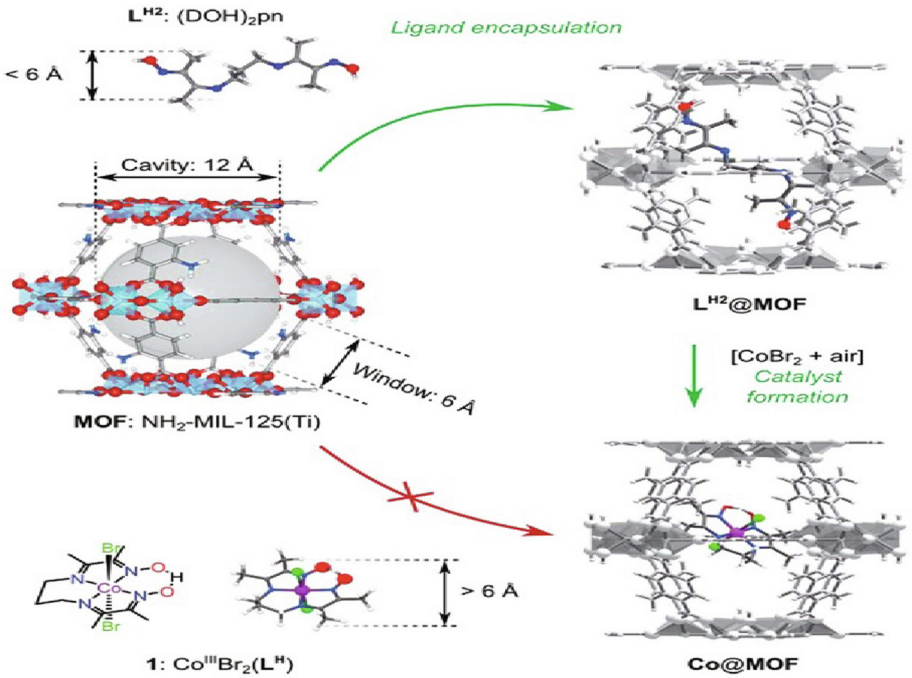

Fig. 7. "Ship-in-a-bottle" synthetic strategy followed for assembling of Co@MOF [95]. Copyright 2015 The Royal Society of Chemistry.

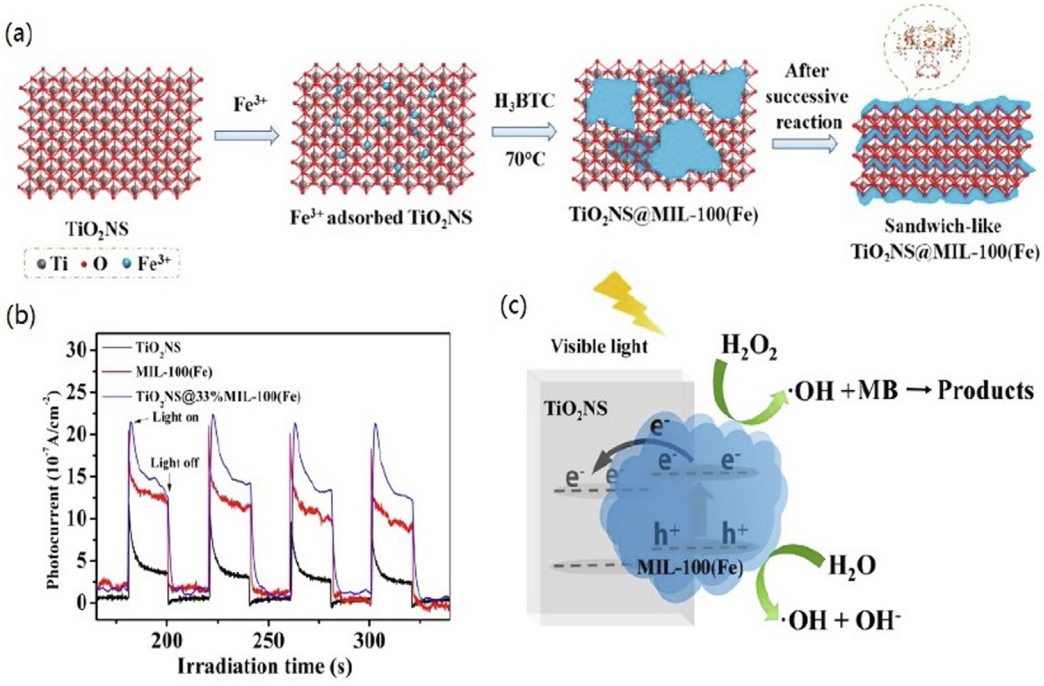

Fig. 8. (a) Synthetic illustration of the preparation procedures for TiO_2NS@MIL-100(Fe). (b) Transient photocurrent response of TiO_2NS, MIL-100(Fe), TiO_2NS@33%MIL-100 (Fe). (c) Proposed mechanism for photocatalytic generation of ·OH over TiO_2@MIL-100(Fe) [114]. Copyright 2017 Elsevier.

4.2.1. Metal oxide doped MILs photocatalysts

Metal oxides have become promising photocatalysts since the unique optical activity and diverse synthetic pathways [103]. However, its photocatalytic efficiency is limited due to the low solar energy utilization efficiency and poor quantum yield caused by the broad band gap [104]. Doping MILs with metal oxide nanoparticles to form heterojunction can broaden the spectral response scope and accelerate the charge separation[105]. TiO_2 is known as an excellent photocatalytic material because of its chemical stability, hypotoxicity and low cost [106]. Many studies have reported the application of TiO_2-MIL in photocatalysis [107–109]. In a related work, Zhao and co-workers [110] prepared NH_2-MIL-125/TiO_2 and showed excellent photocatalytic performance for selective oxidation of cyclohexane by taking advantage of its outstanding ability to harvest light and abundant catalytic sites. The heterojunction structure between NH_2-MIL-125 and TiO_2 can prolong the lifetime of photogenic e^--h^+ pairs. The role of this heterojunction structure of MIL/semiconductor in charge transfer has

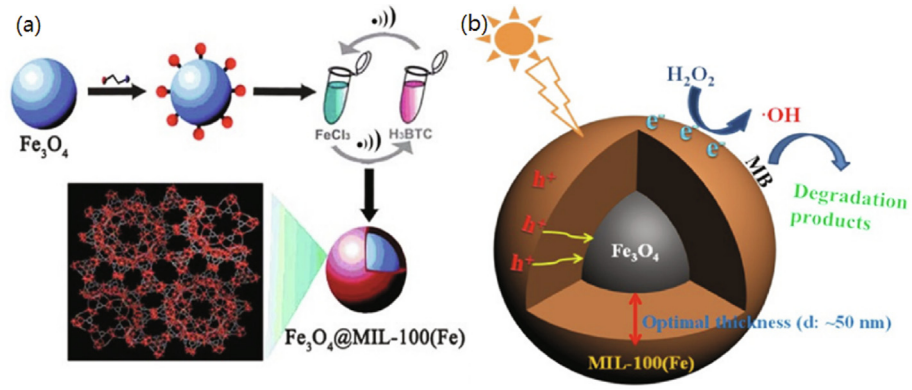

Fig. 9. (a) Schematic illustration of the preparation procedures for Fe_3O_4@MIL-100(Fe) core–shell microspheres [117]. Copyright 2013 The Royal Society of Chemistry. (b) Illustration the possible mechanism for the enhanced photocatalytic ability of Fe_3O_4@MIL-100(Fe) with tunable thickness [116]. Copyright 2015 Wiley-VCH.

been explored by He and co-workers [111]. The introduction of MIL-100(Fe) causes Ti atoms in TiO_2 to be partially replaced by Fe atoms, which leads to significant changes in the band structure of TiO_2, resulting in defective energy levels that act as electron captors. In addition, MIL-100(Fe) provides additional charge transfer and reaction paths. Accordingly, the photodegradation efficiency of tetracycline (TC) was significantly improved.

Some researchers have focused on the fabrication of TiO_2@MIL core–shell architecture as well as the synergistic effects of photocatalysis and absorption of TiO_2@MIL complex. Recently, Sheng and co-workers [112] fabricated TiO_2@MIL-101 double-shell hollow particles and demonstrated TiO_2@MIL-101 can simultaneously absorb and photodegrade H_2S. Similarly, Li et al. [113] constructed the TiO_2@NH_2-MIL-88B(Fe) by a convenient one-step solvothermal process and demonstrated the absorption properties of NH_2-MIL-88B and the photocatalytic properties of TiO_2, which led to an effective improvement for photocatalytic degradation of MB dyes. The MB molecules adsorbed by TiO_2@NH_2-MIL-88B(Fe) in the dark realized the aggregation of the reactants, and then were photodegraded under the light illumination. In addition, the group of Liu [114] altered the morphology of TiO_2 to increase its surface area and absorptive capacity. They incorporated nanosheet-shaped TiO_2 into MIL-100(Fe) to form hierarchical heterostructures through a self-assembly method (see Fig. 8a). The sandwich-like TiO_2NS@MIL-100(Fe) showed an outstanding ability to absorb MB because of the porous channels and ultrahigh surface area. Furthermore, due to the abundant exposed facets of TiO_2, which accelerated the movement of photogenic charges through the interface structure between TiO_2NS and MIL-100(Fe), the TiO_2NS@MIL-100(Fe) showed the strongest photocurrent intensity (see Fig. 8b) and enhanced photocatalytic efficiency for MB degradation as compared to pristine TiO_2NS and MIL-100(Fe). The MIL-100(Fe) in TiO_2NS@MIL-100(Fe) was excited and produced e^--h^+ pairs under visible light illumination, then the movement of photogenerated electrons occurred through the interface structure (see Fig. 8c). On the one site, photogenic h^+ trapped H_2O to form ·OH. On the other site, H_2O_2 reacted directly with MIL-100(Fe) to produce ·OH.

In practical water purification applications, the highly diffuse MIL-based materials are tricky to be separated and recovered. Traditional separation methods such as centrifugal separation or filtration not only reduce the catalytic activity of photocatalysts but also consume energy [115]. The combination of magnetic iron oxide with MILs enables the photocatalysts to be quickly separated from the reaction medium. Nevertheless, iron oxide is easy to photo dissolution. The core–shell structure formed by the magnetic iron oxide embedded in the shell of MILs can effectively prevent Fe_3O_4 from forming exciting radiation[116]. In 2013, Zhang et al. [117] fabricated a magnetic recyclable Fe_3O_4@MIL-100 (Fe) photocatalyst for photocatalytic MB removal (see Fig. 9a). It can be easily separated after many cycles without significant catalytic performance loss. What's more, they revealed that the rate at which h^+ moves toward the Fe_3O_4 core depends on the thickness of the shell. Subsequently, Zhao's team [116] evaluated the effect of thickness of MIL shells in Fe_3O_4@MIL-100(Fe) on photocatalytic performance, and the maximum removal efficiency of MB was obtained when the thickness of MIL shell was about 50 nm (see Fig. 9b). In fact, when the outer layer is too thick, shell-localized h^+ tends to be transferred to the Fe_3O_4 core, which greatly inhibits the photoactivity. Recently, Rasheed and co-workers [115] synthesized MIL-100(Fe) and compounded it with Fe_3O_4 and carbon aerogel (CA). The CA is known for the following two advantages, plenty of active sites resulting from the ultrahigh surface area; porous structure helping absorption of substrates. Consequently, MIL-100(Fe)@Fe_3O_4/CA showed remarkable photocatalytic ability to remove tetracycline hydrochloride. Moreover, due to the addition of magnetic Fe_3O_4, the catalyst can be easily and quickly recycled.

The introduction of Fe_3O_4 is not the only way to obtain magnetic materials. It is a convenient strategy to embed ferric oxide in situ into the MIL framework by reducing metal nodes with the assistance of Na-citrate/NaOAc (see Fig. 10a) [118]. The SEM and TEM images (see Fig. 10b) showed that the Fe_3O_4/MIL-88B(Fe) was nanosheets stacked microspheres with clear edges and abundant interlaced pore structures. The rate of light-induced MB (RhB) dyes removal of Fe_3O_4/MIL-88B(Fe) was 3.46 (2.63) times than that of MIL-88B(Fe). The remarkable photocatalytic activity of Fe_3O_4/MIL-88B(Fe) can be ascribed to two aspects: (1) The doping of Fe_3O_4 leads to the adjustment of the band structure of MIL-88B (Fe), thus broadening the optical response range and increasing the quantum yield. (2) The unique hierarchical structure facilitates the absorption of pollutants and inhibits the recombination of charges.

4.2.2. Metal sulfide doped MILs photocatalysts

Metallic sulfides, an important branch of semiconductor photocatalysts, are attractive because they are abundant and inexpensive materials, and more importantly, they have smaller band gap than metal oxides, which allows them to make better use of solar energy [119–121]. Among the reported metal sulfide photocatalysts, CdS is widely studied on account of its suitable band gap (2.4 eV), which allows it to respond to visible light [122,123]. In the past few years, CdS has been applied to produce H_2 [124], reduce CO_2 [125] and remove organic matters from effluent [126]. However, there are some defects to prevent CdS from being widely employed, such as the rapid charge recombination, the photoerosivity of pristine CdS and the high aggregation of CdS particles [122,127,128]. The combination of CdS and MILs can overcome the

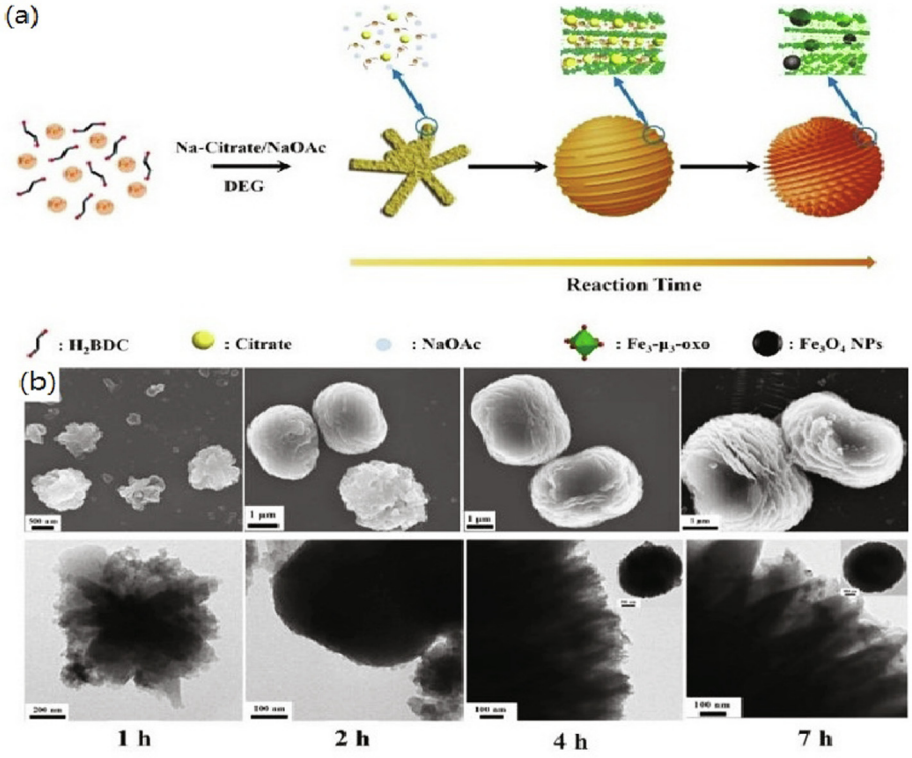

Fig. 10. (a) The corresponding schematic illustration of the evolution process of the NHMMs. (b) The morphology evolution of the NHMMs: typical SEM and TEM images at different reaction time [118]. Copyright 2016 Wiley-VCH.

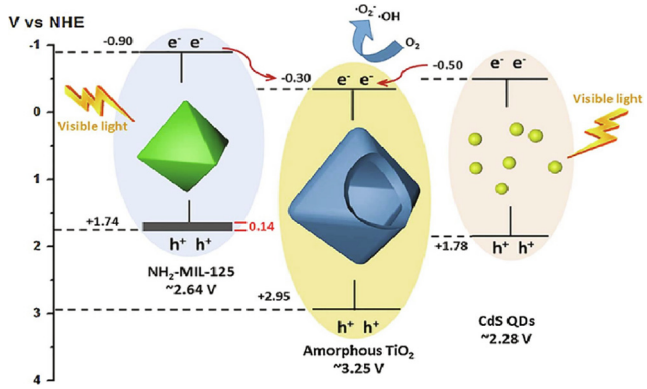

Fig. 11. Possible mechanism of photocatalytic oxidation of NO over CdS/NH_2-MIL-125@TiO_2 catalysts [131]. Copyright 2018 Elsevier.

limitation and promote further development. In 2014, Ke et al. [123] prepared CdS-decorated-MIL-100(Fe) and demonstrated that the photoactivity was significantly improved. In the CdS/MIL-100 (Fe) complex, the photocatalytic efficiency boosted with the weight ratio of MIL-100(Fe) increased since MIL-100(Fe) can reduce the band gap of the CdS as well as improve the absorption of matrix molecules. However, as the weight ratio of MIL-100(Fe) increased further, the photocatalytic efficiency was limited because excessive MILs resulted in the reduction of the effective surface area of CdS and the decrease of photogenerated charge. Thereafter, Wang et al. [129] successfully constructed the ternary composite material Au@CdS/MIL-101. Au NPs were evenly deposited on MIL-101 via double solution method, then CdS was selectively coated on Au NPs. The outstanding photoinduced hydrogen evolution rate (250.0 mol h^{-1}/10 mg) can be summarized as: MILs with ultrahigh surface area allow Au and CdS to be evenly dispersed and provide more catalytic sites; Plasmon resonance absorption of Au NPs broadens the optical response range of hybrid material; CdS facilitates charge movement.

To further improve the photoactivity of CdS/MIL composite, it is feasible to compound CdS QDs with MILs. QDs, as special semiconductors in the size range 2–10 nm, have the advantages of high quantum yield, efficient electron transfer rate and wide light response range [130]. Wu et al. [127] constructed CdS@MIL-101 by the double-solvents strategy. They found the strong interaction between CdS QDs and MIL-101 narrowed the band gap of CdS, which was helpful to boost the photocatalytic ability of CdS@MIL-101. In a prior work, Gao et al. [131] coated TiO_2 on the surface of NH_2-MIL-125, and CdS embedded in NH_2-MIL-125@TiO_2 to fabricate a novel CdS/NH_2-MIL-125@TiO_2 composite material. The thin sheet of TiO_2 covered in the outer layer can protect the photocatalysts from being corroded and poisoned by nitrate and nitrite in the photocatalytic NO removal system, which is responsible for the long lifetime and high stability of CdS/NH_2-MIL-125@TiO_2. Based on the HOMO/LUMO energy of NH_2-MIL-125 and CB/VB of CdS and TiO_2, the mechanism of light-induced removal of NO was proposed as shown in Fig. 11. The superior optical properties of CdS/NH_2-MIL-125@TiO_2 are attributed to the dual excitation pathways, the tight connection, and the matching band potential of NH_2-MIL-125 and CdS QDs. The photoinduced electrons were trapped by O_2 to form $\cdot O_2^-$, which then oxidized NO into HNO_2 and HNO_3. The various components of the composite catalyst exhibited their unique functions: NH_2-MIL-125 with ultrahigh surface area facilitated the absorption of the reactants; the CdS QDs realized the response of visible light; and the TiO_2 served as a buffer to inhibit the recombination of e^- and h^+. Photochemical processes can be summarized by the following equations:

$$\text{catalysts} + \text{visible light} \rightarrow h^+ + e^- \quad (5)$$

$$e^- + O_2 \rightarrow \cdot O_2^- \quad (6)$$

$$\cdot O_2^- + H+ \rightarrow \cdot HO_2 \quad (7)$$

$$e^- + \cdot HO_2 + H^+ \rightarrow H_2O_2 \quad (8)$$

$$H_2O_2 + e^- \rightarrow \cdot OH + OH^- \quad (9)$$

$$h^+ + OH^- \rightarrow \cdot OH \quad (10)$$

$$NO + \cdot OH \rightarrow HNO_2 \quad (11)$$

$$HNO_2 + \cdot OH \rightarrow NO_2 + H_2O \quad (12)$$

$$NO_2 + \cdot OH \rightarrow HNO_3 \quad (13)$$

$$NO + \cdot O_2^- \rightarrow NO_3^- \quad (14)$$

In addition to CdS, other metal sulfides also show good photoactivity, such as In_2S_3, $ZnIn_2S_4$ and MoS_2 [131,132]. Wang and co-workers [133] synthesized a novel core–shell In_2S_3@MIL-125(Ti) for absorption and photocatalytic removal of TC. In In_2S_3@MIL-125(Ti), MIL-125(Ti) core are encapsulated by three-dimensional In_2S_3 sheets. The absorption mechanism of In_2S_3@MIL-125(Ti) can be summarized as the synergistic effect of surface complexation, the π-π interaction between the organic ligands of MIL-125 (Ti) and TC, the hydrogen binding between the μ-OH groups of MIL-125(Ti) and the nitrogen atoms of the TC, and the electrostatic interaction. In a further work, Zhang et al. [134] constructed a layered tandem heterojunction NH_2-MIL-125(Ti)@$ZnIn_2S_4$/CdS, and exhibited excellent photocatalytic activity, with hydrogen generation rate rising to 2.367 mmol $g^{-1}h^{-1}$. This ternary composite structure provides more abundant electron transfer paths. The middle component $ZnIn_2S_4$ as the electron enrichment center accepts electrons from CdS and NH_2-MIL-125(Ti).

1T-MoS_2 as a low-cost and earth-rich metal sulfide is considered as a potential co-catalyst [135]. More importantly, compared with 2H-MoS_2 with only edge active sites, has been proved to have better photocatalytic activity due to abundant active sites on both the edges and the basal planes [136]. Nguyen's team [137] prepared 1T-MoS_2/MIL-125-NH_2 and demonstrated the high-efficiency photocatalytic H_2 production rate compared to that of Pt/MIL-125-NH_2, Co-oxime@MIL-125-NH_2 and Ni_2P/MIL-125-NH_2. More recently, a mild solvent-thermal approach was used to fabricate needle-shaped 1TMoS_2@MIL-53(Fe) by Liu's team [138]. The introduction of 1TMoS_2 lead to narrow band gap and thereby form more active site. Photoelectron was transferred from the surface of MIL-53(Fe) to 1TMoS_2, which facilitated charge separation. It is noteworthy that 1TMoS_2@MIL-53(Fe) showed outstanding recyclability and maintained high photocatalytic activity after five cycles.

4.2.3. Other metal semiconductor doped MILs photocatalysts

Bismuth oxyhalides BiOX (X = Cl, Br, I) have been found to be photoactive under visible light. The BiOX complex consists of $[Bi_2O_2]^{2+}$ slabs, which is sandwiched between double slabs of halogen atoms [139]. This unique layered structure can create electrostatic field by polarizing the associated orbitals and atoms, preventing the photogenerated e^- from recombining with h^+ [140,141]. In 2016, Zhu and co-workers [142] compounded 2D BiOBr materials with NH_2-MIL-125(Ti) to fabricate BiOBr/NH_2-MIL-125(Ti) hybrid for photocatalytic degradation of RhB. The appropriate band gap and heterojunction induced e^- transfer from BiOBr to Ti^{4+}, resulting in better photoactivity of the complex compared with the blank substance. Subsequently, Jahurul Islam and co-workers [140] proposed the mechanism of photodegradation of organic pollutants in water by BiOI/MIL-88B(Fe). Unlike the traditional electron transfer process (i.e., e^- in the CB of MILs transfer toward the CB of semiconductor, while h^+ in the VB of semiconductor move to the MILs), in the BiOI/ MIL-88B(Fe), the e^- in the CB of BiOI moved to the VB of MIL-88B(Fe) and rapidly recombine with h^+ based on the Z-scheme (see Fig. 12). The recombination of e^- and h^+ in the VB of MIL-88B(Fe) promoted the separation of e^--h^+ pair on BiOI. Therefore, plenty of h^+ were left on the VB of BiOI and participated in the oxidation reaction by directly oxidizing organic matter or producing ·OH.

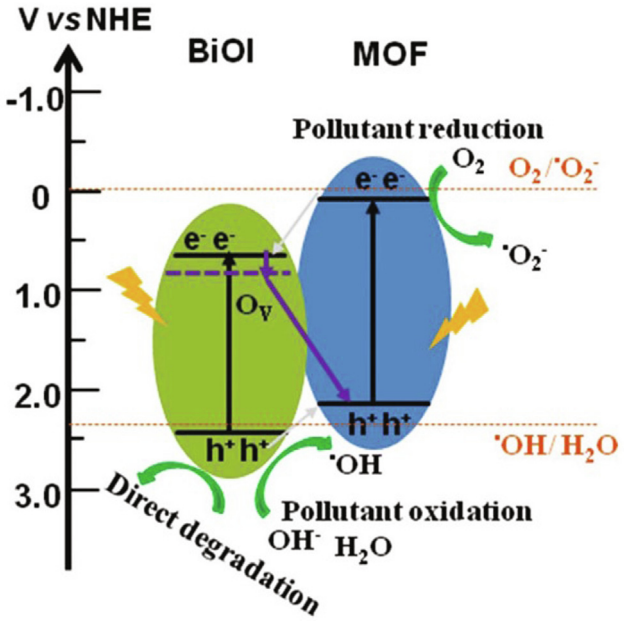

Fig. 12. The mechanism of photocatalysis using the BiOI/MOF nanocomposite involving Z-scheme and oxygen vacancy states [140]. Copyright 2017 The Royal Society of Chemistry.

Direct doping of silver semiconductor is a simple method to optimize the band structure of MILs. For example, silver phosphate (Ag_3PO_4) NPs were well coated on NH_2-MIL-125 to construct Ag_3PO_4@MIL [143]. The reduced bandgap energy of NH_2-MIL-125 (from 2.51 eV to 2.39 eV) and the well-matched heterogeneous interface of Ag_3PO_4@MIL resulted in a 39-fold (35-fold) enhancement of photoactivity in terms of degradation of MB (RhB) compared to TiO_2. Silver vanadate (Ag_3VO_4) and silver tungstate (Ag_2WO_4) were doped to the NH_2-MIL-125 by a similar process [144]. The results revealed that Ag_3VO_4 with better bandgap energy reduction ability (form 2.65 eV to 2.27 eV) is considered as a better candidate for optimizing band structure of MILs.

4.3. On the basis of metal-free semiconductor

Although metal–semiconductor doped MILs have achieved great success in the field of photocatalysis, the metals in metal–semiconductor may be released during the photocatalytic process and cause secondary contamination [15]. In order to avoid the problems caused by metal semiconductor, the strategy of combining non-metal semiconductor with MILs to optimize the performance of photocatalyst has attracted attention.

4.3.1. Graphene-doped MILs photocatalysts

Graphene (GR) as a new 2D carbon material has aroused extensive interests because of their superhigh surface area and effective electrical conductivity [145,146]. Doping MILs with GR or its derivatives (graphene oxide, GO; reduced graphene oxide, rGO) can enhance the charge movement efficiency as well as broaden the spectral response range [145,147]. In 2014, GR/MIL-53(Fe)

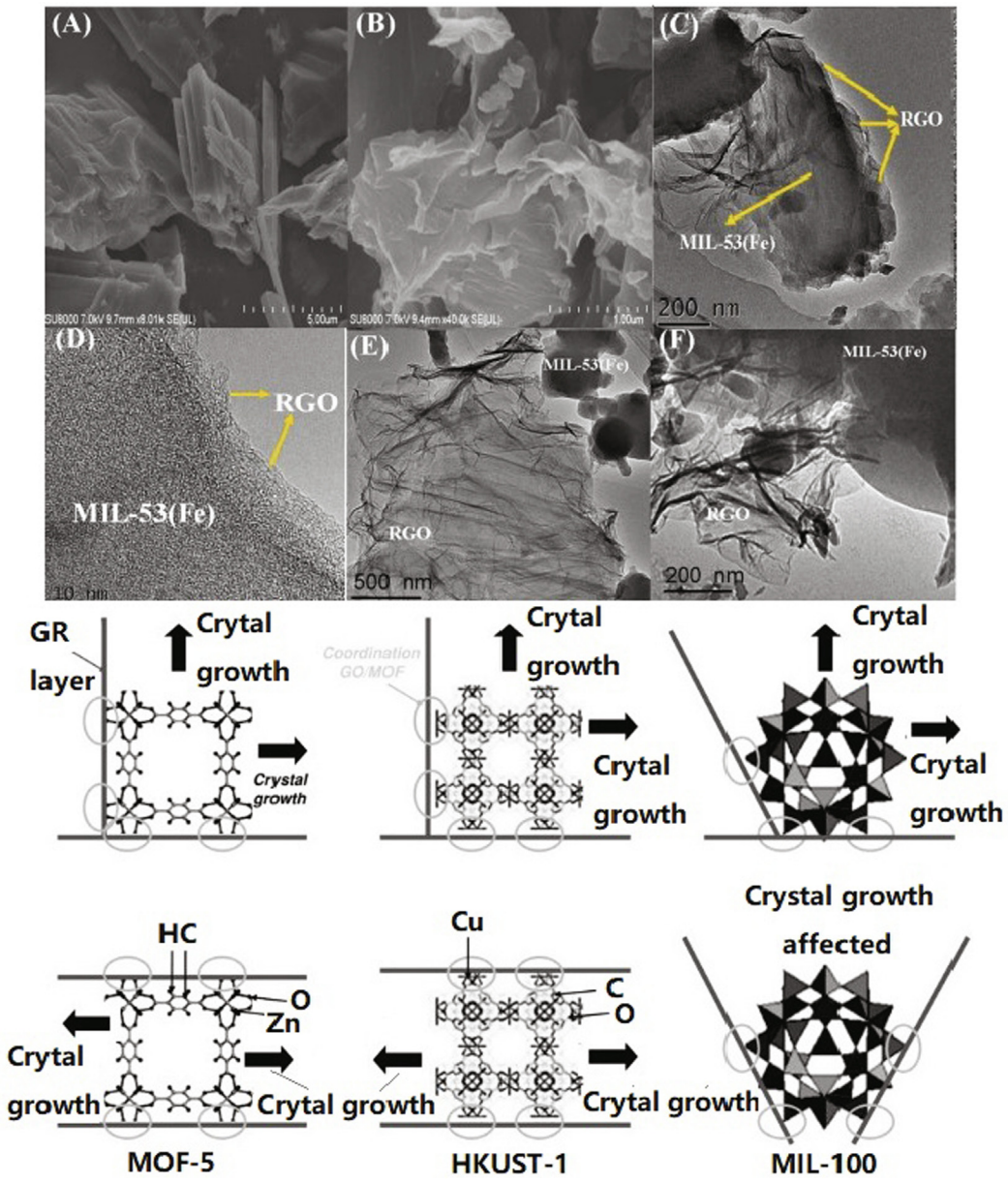

Fig. 13. (a) (A, B) SEM images of MIL-53(Fe) and M53-0.5% RGO, (C, D) TEM and HRTEM images of the M53-0.5% RGO, (E, F) TEM images of the D-M53-0.5% RGO [149]. Copyright 2015 American Chemical Society. (b) Schematic comparison of the coordination between GO carbon layers to the MOF units for different types of MOF network [150]. Copyright 2011 WILEY-VCH.

was hydrothermally hybridized by Zhang et al. [148], and the degradation efficiency of RhB dyes was observably improved. The effects of GR on the photocatalytic activity of GR/MIL-53(Fe) can be summarized as follows: (1) The visible light response characteristics of GR enhances optical absorption intensity of GR/MIL-53(Fe) in the range 500–800 nm; (2) Graphene's excellent electrical conductivity promotes the rapid transfer of photogenerated electrons, thus prolonging the life of the excited charge. In order to seek stronger interface structure between MILs and rGO, Liang and coworkers [149] constructed MIL-53(Fe)-rGO through a simple electrostatic self-assembly approach. As can be observed from Fig. 13a that MIL-53(Fe)-rGO exhibited intimate interfacial contact, which is attributed to the electrostatic self-assembly process. In contrast, only the edges of the MIL-53(Fe) were in contact with rGO in D-MIL-53(Fe)-rGO (obtained by direct solvothermal method), and even some blank MIL-53(Fe) that had no contact with rGO sheet were observed (see Fig. 13a). The random integration in D-MIL-53(Fe)-rGO resulted in poor interfacial contact and charge transfer.

It is worth mentioning that reasonable selection of MILs is necessary to construct GO/MILs. In comparison to MOF-5 and HKSUT-1, MIL-100(Fe) is not an ideal material for preparing GO doped MILs composites [150]. As can be seen from Fig. 13b, the crystals of MOF-5 and HKSUT-1 are cube shape, and the graphene nanosheets are arranged in parallel or perpendicular to each other. In both cases, the MOF-5 and HKSUT-1 grew regularly along the graphene sheet. However, the coordination between the Fe ions of MIL-100(Fe) and the oxygenated group of GO resulted in disordered GO growth. Similar results have been reported in other studies [151,152]. The presence of GO inhibits the possible formation orientation of MIL-101(Fe), resulting in GO@MIL-101(Fe) crystal distortion [152]. On the contrary, MIL-88B(Fe) can be easily wrapped by GO because of its rapid formation kinetics [153]. The catalytic efficiency of MIL-88(Fe)@GO composites was demonstrated to be significantly higher than that of MIL-88(Fe) and GO, MB and RhB were completely degraded within 20 and 30 min, respectively [154].

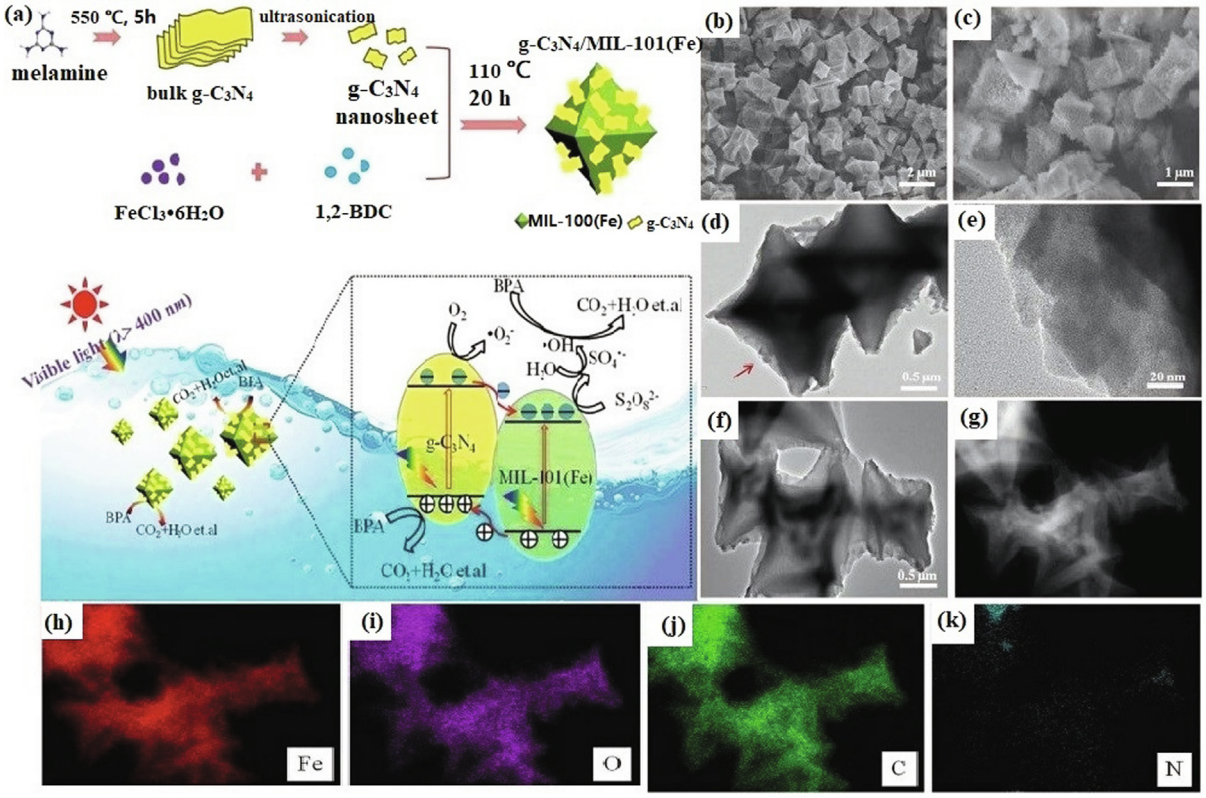

Fig. 14. Schematic illustration of the preparation and proposed photocatalytic mechanism of the g-C_3N_4/MIL-101(Fe) composite. (a,b) SEM images of MIL-101(Fe) and g-C_3N_4/MIL-101(Fe); (c–e) TEM images of g-C_3N_4/MIL-101(Fe); (f-i) HAADF-STEM/EDX mapping of g-C_3N_4/MIL-101(Fe) [163]. Copyright 2018 The Royal Society of Chemistry.

In addition to coating the MILs with two-dimensional graphene sheets, growing MILs on the surface of three-dimensional graphene microspheres has also been reported by Yang [155]. They employed polystyrene microspheres coated with rGO as templates and then removed N, N-dimethylformamide from the core of polystyrene to form empty graphene microspheres. Subsequently, NH_2-MIL-53(Al) crystals were grown on the surface of the empty microspheres to construct NH_2-MIL-53(Al)/rGO with unique spherical structure. The hollow microsphere structure of NH_2-MIL-53 (Al)/rGO exhibited outstanding light harvesting properties because of the scattering of light in the microsphere cave. Consequently, the efficiency of photodegradation of MB was improved.

4.3.2. Graphitic carbon nitride-doped MILs photocatalysts

As an attractive candidate for photocatalytic materials, graphitic carbon nitride (g-C_3N_4) has aroused keen interest because of the desired band-gap width (2.70 eV) and stability over a wide pH range (0–14) [156–159]. However, the photocatalytic efficiency of g-C_3N_4 is not satisfactory since the poor charge separation capability and confined active sites [160]. Fortunately, the g-C_3N_4 has a flexible architecture that makes it easy to contact and encapsulate on other substrates or base materials. Among them, the combination of g-C_3N_4 and MILs is a promising method to enhance photoactivity via improving light absorption capacity, increasing surface area and active sites [161]. For example, compared to pure MIL-125(Ti) and g-C_3N_4, g-C_3N_4/MIL-125(Ti) exhibited outstanding photocatalytic performance, and the photoinduced removal efficiency of RhB was 2.1 and 34 times higher, respectively [162]. Subsequently, Gong et al. [163] successfully prepared g-C_3N_4/MIL-101 (Fe) via a two-step process. As shown in Fig. 14a, in the first step, bulk g-C_3N_4 was stripped off under ultrasonication treatment to form g-C_3N_4 nanosheet. In the second step, the obtained g-C_3N_4 nanosheet and MIL-101(Fe) precursor were mixed to prepare g-C_3N_4/MIL-101(Fe) through a hydrothermal approach. SEM figures (Fig. 14b,c) reveal that the load of g-C_3N_4 hardly changed the morphology of MIL-101(Fe), and MIL-101(Fe) still maintain the octahedral structure. According to TEM images (Fig. 14d–f), g-C_3N_4 is tightly attached to the surface of MIL-101(Fe). The HAADF-STEM image (Fig. 14g) and the Fe, O, C and N elements mapping images (Fig. 14h–k) clearly illustrate that these elements are evenly distributed in g-C_3N_4/MIL-101(Fe), which verify that the g-C_3N_4 is well distributed on MIL-101(Fe). The light-induced catalytic efficiency of g-C_3N_4/MIL-101(Fe) was greatly improved and almost 98% of bisphenol A (BPA) was removed within 60 min. Very recently, Dao et al. [164] have successfully applied NH_2-MIL-101 (Fe)/g-C_3N_4 in the field of energy regeneration. The photocatalytic CO_2 reduction rate of NH_2 MIL-101(Fe)/g C_3N_4 was 3.6 and 6.9 times higher than that of NH_2-MIL-101(Fe) and sole g-C_3N_4, and the highest CO production rate reached 132.8 μmol g^{-1}. Moreover, the solution-free reaction strategy not only improves the absorption capacity of photocatalyst to CO_2, but also enhances its selectivity to produce gas products.

Interface contact by wrapping the stripped g-C_3N_4 around the surface of MILs is known to be weak. To obtain intimate interface contact between MILs and g-C_3N_4, a simple grinding process was used by Bai et al. [165] to synthesize g-C_3N_4-MIL-53(Fe). This grinding method formed close interface contact between MIL-53 (Fe) and g-C_3N_4, as well as provided abundant active sites for H_2 production by splitting water. In order to seek more compact heterogeneous structures, the group of Huang [166] added g-C_3N_4 to a hot concentrated HNO_3 solvent to form protonized colloidal species (C_3N_4-H^+) which easily coated on the outer surface and cavity of MIL-100(Fe). The coating effect was then formed between MIL-100(Fe) and C_3N_4-H^+ through the thermolysis

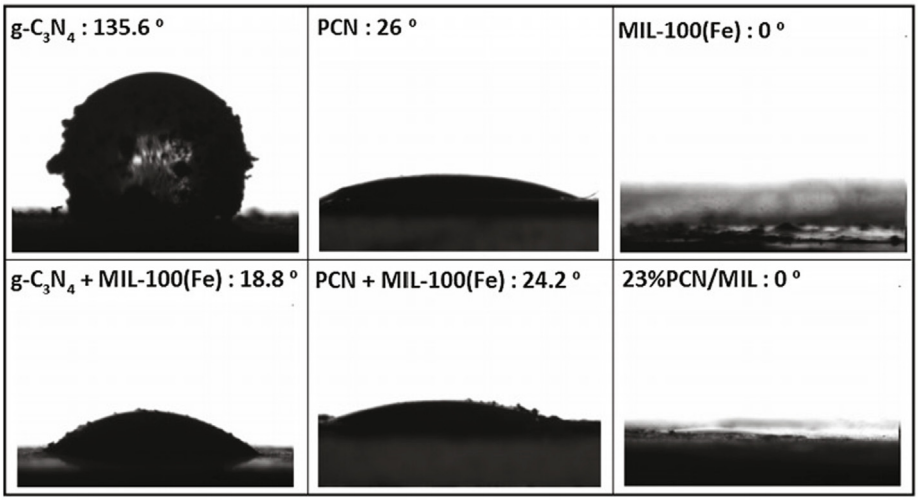

Fig. 15. Contact angle images of g-C_3N_4, PCN, MIL-100(Fe), mechanically mixed g-C_3N_4 + MIL-100(Fe), mechanically mixed PCN + MIL-100(Fe) and 23%PCN/MIL [166]. Copyright 2018 Elsevier.

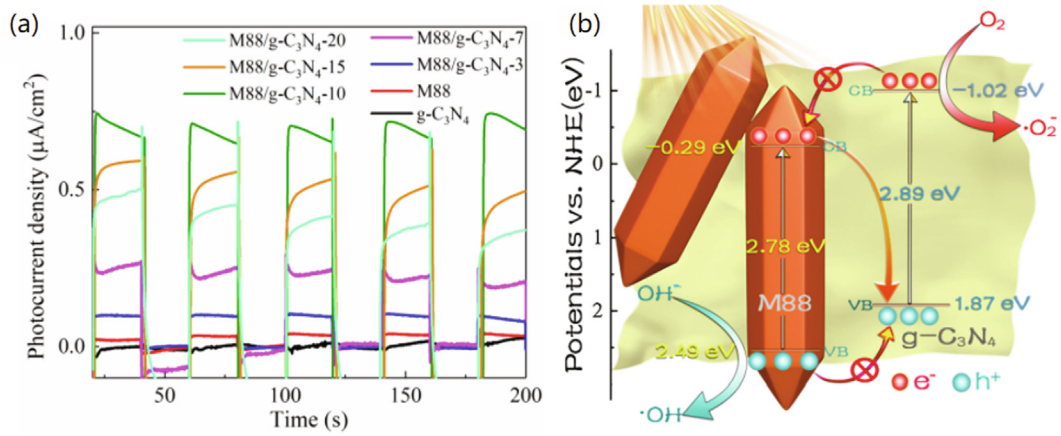

Fig. 16. (a) Transient photocurrent response of g-C_3N_4, MIL-88A and MIL-88A/g-C_3N_4 composites. (b) Schematic illustration of photocatalytic mechanism of M88/g-C_3N_4 under visible light irradiation [171]. Copyright 2019 Elsevier.

treatment at 150 ℃. They confirmed that protonized g-C_3N_4 (PCN) was successfully coated on MIL-100(Fe) by measuring the contact angle. As exhibited in Fig. 15, g-C_3N_4, PCN, MIL-100(Fe), and physically mixed g-C_3N_4 and MIL-100(Fe) all showed convex angles because of their hydrophobicity, whereas the contact angle of pure MIL-100(Fe) was 0° due to the strong hydrophilic properties. Similarly, PCN/MIL also exhibited a perfectly flat contact angle. This result indicated that the protonated g-C_3N_4 was completely grafted onto MIL-100(Fe). Coating MIL-100(Fe) with protonated g-C_3N_4 can also adjust the surface area of the complex and the size of MIL-100(Fe) matrix to the most suitable value to achieve the best photocatalytic efficiency.

The photocatalytic efficiency of MOF/g-C_3N_4 hybrid can be further improved by introducing suitable co-catalyst. In 2015, Su et al. [167] successfully synthesized NH_2-MIL-125(Ti)/Pt/g-C_3N_4 hybrid with a three times enhancement of photocatalytic H_2 production activity compared to Pt/g-C_3N_4. In a following work, Xu et al. [168] deposited NiPd nanoparticles onto NH_2-MIL-125(Ti)/g-C_3N_4 to obtain NH_2-MIL-125(Ti)/CN/NiPd. In the case of EY as photosensitive agent, the photocatalytic H_2 production rate of NH_2-MIL-125(Ti)/0.75CN/$Ni_{15.8}Pd_{2.1}$ was significantly increased (8.7 mmol g^{-1}-h^{-1}) because EY and NiPd enable photocatalysts to gain stronger light harvesting capabilities.

In addition, some studies have reported other multiplex hybrid complexes. In a related work, Li and co-workers [169] grew NH_2-MIL-53(Fe) crystals on g-C_3N_4-doped pyromellitic diimide (g-C_3N_4/PDI) layer via in-suit strategy to synthesize g-C_3N_4/PDI@MOF. The photocatalytic efficiency of the CPM-2 (the weight content of the g-C_3N_4/PDI is 75%) was much higher than that of g-C_3N_4@NH_2-MIL-53(Fe), indicating that the existence of PDI could boost the photoactivity. The strong electron affinity of PDI can shift the oxidation and reduction potentials of g-C_3N_4, which lead to a better match between NH_2-MIL-53(Fe) and g-C_3N_4/PDI. Moreover, they assessed the influence of ions such as Ca^{2+}, K^+, Mg^{2+}, Na^+, Cl^-, SO_4^{2-}, NO_3^- and HCO_3^- which co-existed with the target pollutant in the actual water. The results showed that Cl^- played an adverse role, SO_4^{2-} promoted the generation of effective free radicals, and other ions had no significant effect during the photocatalytic removal of TC.

Recently, the Z-scheme heterojunction formed by the combination of MILs and g-C_3N_4 has gained increasing interest because of its wide light absorption range, strong reducibility, and efficient charge separation. Zhou et al. [170] combined NH_2-MIL-125(Ti) with benzoic acid functionalized g-C_3N_4 (CFB) to establish Z-scheme heterojunction through covalent band. The bonding of hydroxyl oxygen atoms in CFB and Ti atoms in NH_2-MIL-125(Ti)

Table 4
Summary of MILs-derived photocatalysts.

MIL	Template	Structure/ Morphology	Light source	Photocatalytic performance	Mechanism	Recycled times	Ref.
TiO_2	MIL-125(Ti)	Uniform cake-like cylindrical structure	UV	As(III) was oxidized	h^+, $\cdot O_2^-$, ·OH	4	[179]
TiO_x/C	MIL-125(Ti)	/	/	MB was degraded	/	/	[184]
TiO_2@C-N(x)	NH_2-MIL-125	Caky shape	Visible	The mineralization efficiency reached 51.9% at 62.4% of styrene degradation within 240 min	$\cdot O_2^-$, ·OH	/	[185]
GNP/TiO_2	NH_2-MIL-125	/	UV	Heterogeneous CO_2/H_2O reduction to CH_4	/	2	[186]
Pd/TiO_2	NH_2-MIL-125(Ti)	Hierarchical porous structure	UV–vis	The rate of H_2 evolution reached 979.7 mol h^{-1}	/	/	[187]
Pd/TiO_2	NH_2-MIL-125(Ti)	/	Sunlight	The rate of H_2 evolution reached 112.7 mol h^{-1}	/	3	
Cu/TiO_2	MIL-125(Ti)	Porous nanostructure	Sunlight	Photocatalytic CO_2 reduction with water vapor	/	5	[188]
TiO_2@N-doped porous carbon	NH_2-MIL-125(Ti)	Butterfly-like structure	Visible	Selective oxidation of amines to imines	$\cdot O_2^-$	/	[189]
γ-Fe_2O_3/TiO_2	MIL-53(Fe)	Sphere-like shape	UV	Almost 100% of 20-ppm MB and MO were degraded	$\cdot O_2^-$, ·OH	/	[190]
Fe_2O_3@TiO_2	MIL-101(Fe)	Core-shell heterostructure	Visible	The rate of H_2 evolution reached 0.625 μmol $mg^{-1}h^{-1}$	/	3	[191]
Fe_2O_3-TiO_2-PtO_x	MIL-88B	Core-shell heterostructure	Visible	The rate of H_2 evolution reached 22 mmol h^{-1}	/	5	[192]
Fe@C	MIL-101(Fe)	Core-shell structure	Sunlight	The maximum reaction rates for the conversion of CO_2 reached 26.12 mmol h^{-1} g^{-1}	/	/	[193]
CdS	MIL-53(Al)	Hierarchical porous structure	Visible	The rate of H_2 evolution reached 634.0 μmol $g^{-1}h^{-1}$	/	4	[194]
ZnO	MIL-53(Al)	Nanosheets	UV	98.15% MO was removed	$\cdot O_2^-$, ·OH	/	[195]
In_2S_3	MIL-68-In	Hexagonal nanorod-like structure	Visible	97% MO and 66% TC were degraded for 120 min	h^+, $\cdot O_2^-$	/	[196]
In_2S_3-$CdIn_2S_4$	MIL-68	Hierarchical heterostructured nanotubes	Visible	Photoreduction of CO_2 produces CO at a rate of 825 μmol h^{-1} g^{-1}	/	6	[197]

makes benzoic acid act as a bridge between MILs and g-C_3N_4, which can accelerate photocharge transfer. Later, Shao et al. [171] synthesized a series of MIL-88A/g-C_3N_4 with different mass ratios of the MIL-88A for photoinduced degradation of RhB. As shown in the photocurrent spectrum (see Fig. 16a), the MIL-88A/g-C_3N_4-10 (mass ratios of the MIL-88A for 10%) exhibited the most outstanding photocatalytic properties, with the rate of catalytic degradation of dyes reaching almost 100% after 30 min under light exposure. The mechanism of photocatalysis is shown in Fig. 16b. Different from the charge transfer path of traditional heterojunction, e^- in the CB of MIL-88A moved to the VB of g-C_3N_4 and recombined with h^+ in the VB of g-C_3N_4 in the Z-scheme photocatalysts. Consequently, the e^- in the CB of g-C_3N_4 and the h^+ in the VB of MIL-88A were effectively separated.

4.3.3. Other metal-free semiconductor doped MILs photocatalysts

As green and safe substrate, carbon nanomaterials with high conductivity and superior light absorption can be doped into MILs to construct environmentally friendly photocatalysts with high performance [172]. For example, carbon nanodots (CDs) doped NH_2-MIL-88B possesses excellent charge separation performance because CDs can serve as electron acceptors to promote charge transfer [173]. In addition, the band structure of MILs can be regulated by the carbon nanotubes and carbon quantum dots, thus upregulating the light absorption boundary of the doped MILs, which has practical advantages in natural water evolution [174,175].

Chang et al. [176] coated the MIL-100(Fe) on silicon dioxide (SiO_2) to prepare SiO_2/MIL-100(Fe) via a simple layer-by-layer process. Excellent dyes adsorption ability and dispersed MIL-100(Fe) resulted in increased photocatalytic activity of SiO_2/MIL-100(Fe) and 94% RhB was removed within 90 min. The ultra-high surface area, which is thought to be responsible for the increased dyes absorption capacity, may be caused by two factors. First, the MIL-100(Fe) increases the surface roughness of the composite photocatalyst. Second, the MIL-100(Fe) coated on the surface of SiO_2 has a large surface area. Furthermore, the core–shell fibre-membrane structure of SiO_2/MIL-100(Fe) is easily recycled and can be put into the next cycle after a simple rinse.

5. MILs-derived photocatalysts

Structurally, the modified or doped MOFs can still maintain the original structure, while the photocatalyst derived from MOFs destroys the original framework to form a new composite material. MOFs derived materials inherit the characteristics of large surface area and high porosity of parent materials, and more importantly, improve the disadvantages of weak coordination bonds between metal nodes and organic ligands in MOFs and shorten the distance of electronic transport [177,178]. Therefore, the photocatalysts derived from MOFs have better stability and conductivity. The photocatalytic properties of different metal-based MILs derivatives are also very different. In addition to the original MILs as template, the modified MILs pyrolysis products integrate the properties of different units. Some representative MILs-derived photocatalysts and their corresponding properties are listed in Table 4.

5.1. Ti-based MILs as template

The optimization of the photoactivity of TiO_2 has always been a research hotspot in the field of photocatalysis. In recent years, TiO_2 nanocrystals derived from Ti-based MILs have aroused widespread

interest [179,180]. In addition to inheriting the high porosity of the template MILs, the derived TiO_2 also possesses superior photocatalytic activity, such as the outstanding light harvest capacity and rapid charge movement. Direct pyrolysis of Ti-based MILs provides a simple and effective way to prepare porous TiO_2. In addition, various methods such as introducing hybrid atoms and loading with other materials to modify MILs before calcination can further improve the performance of photocatalyst.

In general, direct pyrolysis of Ti-MIL in oxygen or air conditions results in decomposition of organic ligands and the formation of porous TiO_2. Liu et al. [179] obtained cake-like TiO_2 by calcinating MIL-125(Ti) for photocatalytic As(III) removal. The high As(III) removal capacity of MIL-125(Ti)-derived TiO_2 is attributed to its long charge life and high As(V) adsorption capacity. The calcination temperature can control the crystal phase of TiO_2, and anatase TiO_2 gradually transforms into anatase/rutile mixed phase TiO_2 with the increase of temperature. It has been reported that anatase/rutile mixed phase TiO_2 has been shown to be more photoactive because of the presence of stepped energy level structure, which leads to more efficient charge separation [180–182]. Surprisingly, anatase TiO_2 formed by calcining MIL-125(Ti) at 380 ℃ achieved the best degree of As(III) removal than anatase/rutile mixed phase TiO_2 calcined at higher temperatures [179].

The combination of TiO_2 and carbon can provide large specific surface area and fast charge transfer channel. Unfortunately, traditional integration methods tend to form weak interface contacts, which leads to unsatisfactory photocatalytic performance [183]. In view of this, carbon supported TiO_2 obtained by direct pyrolysis of Ti-MIL in an inert atmosphere was considered. The coordination bonds between the linkers and the metal nodes of Ti-MIL make the pyrolyzed TiO_2 and carbon close contact, thereby TiO_x/C pyrolyzed by MIL-125(Ti) showed excellent photocatalytic degradation of MB [184]. Interestingly, NH_2-MIL-125(Ti)-derived amorphous carbon was decomposed to form more and larger pores to accelerate photogenic charge transfer after CO_2 annealing treatment [185].

Pre-synthetic modification is a necessary means to fabricate different porous materials. Based on this strategy, Kira and co-workers [186] deposited gold nanoparticles (GNPs) on NH_2-MIL-125 and then pyrolyzed the GNP/NH_2-MIL-125 nanocrystals to produce GNP/TiO_2. The high light absorption capability of surface plasmon of gold nanoparticles in GNP/TiO_2 contributes to the significant improvement of photoactivity as compared to traditional TiO_2. Similar results have also been reported by Yan et al. [187], the coupling of precious metal Pd with derived TiO_2 can form Schottky heterojunctions to increase electron transfer rate and the number of active sites, and the optical response range of Pd/TiO_2 has also been widened. Recently, Li et al. [188] synthesized derived Cu/TiO_2 with Cu-Co loaded MILs as template precursor, and proved that the catalytic activity of derived Cu/TiO_2 was greatly improved. More importantly, the photocatalytic reduction of CO_2 over Co-Cu/TiO_2 produced not only CO and CH_4 but also high-value hydrocarbons (C_{2+}) after cobalt doping. The improved photocatalytic performance of Co-Cu-MIL is attributed to: (1) Co-Cu doping causes the light absorption range to shift to the visible region; (2) Cu species promotes electron transfer from Ti to Cu; (3) Co species promotes the migration of photogenerated holes and optimizes the selectivity of the reaction, thus generating more C_{2+} hydrocarbons.

Moreover, different heteroatoms can be doped into carbon/TiO_2 by reasonable selection of MILs and pyrolysis conditions. Among them, doping N can reduce the band gap energy of TiO_2, thus optimizing its optical properties. For example, Wang et al. [189] successfully synthesized TiO_2@N-doped porous carbon using NH_2-MIL-125(Ti) as the sacrificial template. The introduction of N and C leads to the light absorption range to redshift. The high surface area of porous carbon enables the uniform dispersion of TiO_2 NPs and the good conductivity of carbon materials promotes the rapid transfer of electrons. Consequently, the photocatalytic performance of modified TiO_2 showed a dramatic improvement with 99% imine yield.

5.2. Fe-based MILs as template

Fe-based MILs derivatives are usually assembled as building blocks on different substrates or coated with other materials for targeted applications. The surface-active site of TiO_2 can be modified by incorporation of MIL-53(Fe)-derived γ-Fe_2O_3 [190]. Photocatalytic results showed that MB and MO could be completely degraded over MIL-53(Fe)-derived γ-Fe_2O_3/TiO_2 within 50 min. Lin and co-workers [191] coated nanoscale MIL-101(Fe) with amorphous TiO_2, then calcined to form Fe_2O_3@TiO_2 crystals (see Fig. 17a). The calcined hybrid material maintains an octahedral structure due to the TiO_2 shell as a support for Fe_2O_3 particles. The suitable band energy of TiO_2 and visible light response of Fe_2O_3 enable Fe_2O_3@TiO_2 to produce H_2 from water splitting using visible light. With the assistance of K_2PtCl_4, the H_2 production over Fe_2O_3@TiO_2 reached 30 μmol mg^{-1} and increased linearly within 48 h (see Fig. 17b). Subsequently, Pham et al. [192] coated the TiO_2 on MIL-88B(Fe) and then calcined it to form Fe_2O_3-TiO_2-PtO_x crystals with H_2PtCl_6 as a Pt source. The thickness of TiO_2 shell can be controlled by the concentration of Titanium(IV)-(triethanolaminato) isopropoxide $C_3H_7OTi(OC_2H_4)_3N$ (TEAI) grafted onto MIL-88B, and the thickness increases with the increase of concentration of TEAI within a certain range (6 mM to 50 mM).

The incorporation of graphene into the metal substrate not only optimizes the properties of the photocatalysis, but also produces a constraint effect different from the behavior of blank nanoparticles. For example, the MIL-101(Fe)-derived Fe@C constructed with Fe NPs encapsulated in ultrathin carbon layers can produce a constraint effect to promote CO release, thus achieving high selectivity to CO (see Fig. 17c) [193]. In addition, the combination of photothermal effect and local plasmon resonance effect of Fe NPs are beneficial to the formation of surface carriers of Fe NPs and the excitation of CO_2 as well as providing appropriate energy for the reaction. Consequently, Fe@C outperformed all the control samples (Fe/SiO_2, Fe/carbon nanotube, and carbon nanotube) in terms of photocatalytic CO_2 reduction, and the CO yield of Fe@C reached 2196.17 μmol within 120 min (see Fig. 17d).

5.3. Al-based MILs as template

Removing MILs after introducing guest into MILs pore is an important method for preparing target porous catalysts. The MIL-53(Al) with high thermal stability and breathing pore structure is an ideal host [194]. Xiao et al. [194] introduced Cd-containing nitrate into MIL-53(Al) and formed CdO/MIL-53(Al) after calcination, and then used Na_2S to achieve the conversion from CdO to CdS. Finally, the chemical instability of MIL-53(Al) makes it easy to be removed under NaOH treatment to obtain porous CdS. The H_2 production rate of MIL-53(Al)-derived CdS reached 634.0 μmol $g^{-1}h^{-1}$ under visible light irradiation, which was 2 and 5 times higher than that of bulk CdS and nano CdS, respectively. Recently, Xiao and co-workers [195] successfully prepared ZnO using Zn-free MOF (MIL-125(Ti) and MIL-53(Al)) as template by one-pot hydrothermal method. Zinc acetate as a Zn source was introduced into Zn-free MOFs and then calcined to form ultrafine nanocrystals ZnO. MIL53-ZnO exhibits larger pore volume than MIL125-ZnO, which contributes to the formation of surface-reactive species and effective mass transportation. Furthermore, ZnO obtained by the MOFs reaction template method introduced many oxygen defects, which resulted in a reduced band gap and increased light absorption capacity. The results showed that the

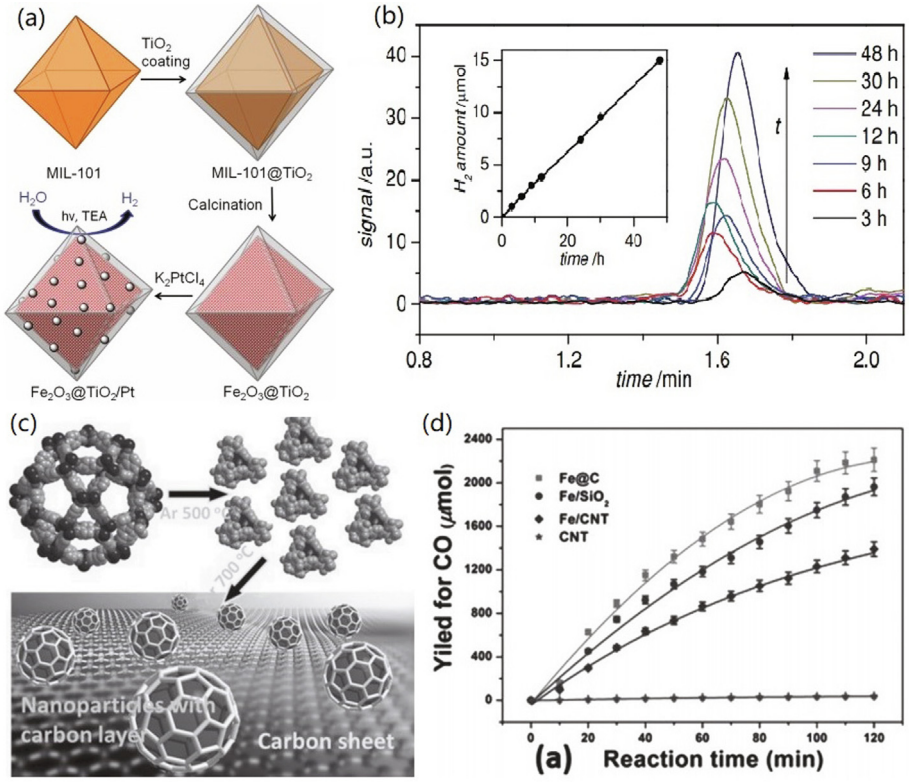

Fig. 17. (a) MOF-templated synthesis of Fe_2O_3@TiO_2. (b) H_2 produced by Fe_2O_3@TiO_2 over 48 h, with a 420 nm filter [191]. Copyright 2012 WILEY-VCH. (c) Schematic illustration for the two-step preparation process for the core–shell structured Fe@C hybrid. (d) Photoinduced CO_2 conversion performance for Fe@C, Fe/SiO_2, Fe/CNT, and CNT catalysts [193]. Copyright 2016 WILEY-VCH.

photodegradation rate of MO over MIL53-ZnO and MIL125-ZnO reached 98.15% and 96.89%, respectively.

5.4. In-based MILs as template

The preparation of porous metal sulfide nanostructures using MILs as precursors is usually achieved through sulfidation with various sulfur sources. For example, Fang et al. [196] successfully synthesized hollow In_2S_3 through sulfidation treatment using MIL-68(In) as template, and the hollow In_2S_3 nanorods have excellent photocatalytic ability to degrade TC and MO. Additionally, Wang and co-workers [197] utilized MIL-68(In) as template to fabricate In_2S_3 nanotube and then converted In_2S_3 into hierarchical heterostructured In_2S_3-$CdIn_2S_4$ by cation exchange method. The hollow hierarchical heterostructured structure of In_2S_3-$CdIn_2S_4$ reduced the migration distance of photogenic carriers, improved the absorption capacity of CO_2, provided abundant surface-active sites, and enhanced the ability of capturing light. These advantages resulted in a 12-fold increase of CO_2 photoreduction activity compared to In_2S_3 material and the highest rate of CO production reached 825 μmol

6. Concluding remarks and prospects

Herein, the recent progress of MIL-based materials for photocatalytic applications are reviewed. The ultrahigh surface area, excellent porosity and compatible structure bring the MILs as photocatalysts to the attention of researchers. Among the strategies of enhancing the performance of MIL-based photocatalysis, many studies have focused on development of functionalized MILs (modification of MILs, doping of MILs based on metal nanoparticles, metal semiconductor and metal-free semiconductor, and the derivatives of MILs). These strategies are based on the photocatalytic mechanism to improve the performance of MIL based photocatalysts from three aspects: optimizing optical properties, improving electron transfer rate, and accelerating surface catalytic reactions. Structurally, both modified MILs and MILs complexes retain their original crystalline structures, but the MIL derivatives generally changed the original frame structure. In addition, the addition of oxidizer (e.g., H_2O_2, PS) or photosensitizer (e.g., RhB, Erythrosin B and Eosin Y) can also enhance the photocatalytic performance. Although the MIL-based materials have bright future, there are still many challenges to put it into practice.

(1) It is well known that the properties of MILs with flexible framework can be regulated by introducing substituent groups to linkers, or by changing or doping the metal ions/-clusters on the nodes. However, there are few reports on the modification of organic ligands or metal nodes of MILs. More researches are needed to develop various structures of the MILs to further improve its photocatalytic performance and stability.
(2) The coordinated structure of MILs enables the introduction of multifunctional modules into a single frame structure for collaborative catalysis, which makes it possible to construct different types of MIL-based composite photocatalysis with multiple functions. However, the structure of most complex MIL-based materials is not clear, which greatly hindered the exploration of structure–property-performance relationship. Therefore, it is necessary to explore the morphology of the different components, as well as the interface properties between the MILs and the secondary components.

(3) Applications of MIL-based photocatalysts in the energy field focus on water splitting and CO_2 reduction. Despite the increasing reports in recent years, there are still a series of problems to be solved. Currently reported MIL-based photocatalysts have a very limited ability to reduce CO_2 and H_2 evolution and are dependent on sacrificial agents, which is not economical and environmentally friendly. In order to conform to the reality and avoid the use of sacrificial agents, it is urgent to combine oxidation side reactions such as oxygen evolution with reduction reactions. In addition, single atoms can be used as cocatalyst for hydrogen evolution instead of precious metals.

(4) At present, the researches of MILs as photocatalysts are still in the laboratory stage. The catalytic efficiency is not only related to the properties of the photocatalysts themselves, but also influenced by the actual environment. In the real environment, it is faced with ion interference, pH and temperature discomfort. The following research should focus on the interaction between MIL-based photocatalysis and environment, and broaden the application conditions of MILs. Moreover, stability and reusability are the non-negligible factors for MIL-based materials to be put into practical application. Therefore, more research is needed to explore the causes and conditions of structural collapse of MILs photocatalyst. Since there is no clear step for the synthesis of high-stability MILs, it is necessary to explore simple and practical synthetic conditions for the construction of stable structures of MILs.

(5) So far, the photocatalytic mechanism based on MILs is not clear. Therefore, it is of great significance to further explore the photocatalytic mechanism of MILs through experiments and theoretical calculations for the design of efficient photocatalysts. In addition, some advanced characterization techniques are needed in this field to fully understand the photocatalytic mechanism.

Declaration of Competing Interest

The authors declare that they have no known competing financial interests or personal relationships that could have appeared to influence the work reported in this paper.

Acknowledgements

This study was financially supported by the Program for the National Natural Science Foundation of China (51909084, 51909085, 51579098, 51679085, 51779090, 51521006), the National Program for Support of Top-Notch Young Professionals of China (2014), the Program for Changjiang Scholars and Innovative Research Team in University (IRT-13R17), China Postdoctoral Science Foundation Funded Project (2018 M642977), the Three Gorges Follow-up Research Project (2017HXXY-05) and the Fundamental Research Funds for the Central Universities (531118010247).

References

[1] M. Cheng, G. Zeng, D. Huang, C. Lai, Y. Liu, C. Zhang, R. Wang, L. Qin, W. Xue, B. Song, S. Ye, H. Yi, J. Colloid Interface Sci. 515 (2018) 232–239.
[2] L. Li, C. Lai, F. Huang, M. Cheng, G. Zeng, D. Huang, B. Li, S. Liu, M. Zhang, L. Qin, M. Li, J. He, Y. Zhang, L. Chen, Water Res. 160 (2019) 238–248.
[3] T.-Y. Tan, Z.-T. Zeng, G.-M. Zeng, J.-L. Gong, R. Xiao, P. Zhang, B. Song, W.-W. Tang, X.-Y. Ren, Sep. Purif. Technol. 235 (2020) 116167.
[4] S. Ye, G. Zeng, H. Wu, J. Liang, C. Zhang, J. Dai, W. Xiong, B. Song, S. Wu, J. Yu, Resour. Conserv. Recycl. 140 (2019) 278–285.
[5] X. Zhou, Z. Zeng, G. Zeng, C. Lai, R. Xiao, S. Liu, D. Huang, L. Qin, X. Liu, B. Li, H. Yi, Y. Fu, L. Li, Z. Wang, Chem. Eng. J. 383 (2020) 123091.
[6] Y. Liu, G. Zeng, H. Zhong, Z. Wang, Z. Liu, M. Cheng, G. Liu, X. Yang, S. Liu, J. Hazard. Mater. 322 (2017) 394–401.
[7] Y. Liu, M. Cheng, Z. Liu, G. Zeng, H. Zhong, M. Chen, C. Zhou, W. Xiong, B. Shao, B. Song, Chemosphere 236 (2019) 124387.
[8] F. Qin, Y. Peng, G. Song, Q. Fang, R. Wang, C. Zhang, G. Zeng, D. Huang, C. Lai, Y. Zhou, X. Tan, M. Cheng, S. Liu, J. Hazard. Mater. 398 (2020) 122816.
[9] W. Xing, M. Zhang, J. Liang, W. Tang, P. Li, Y. Luo, N. Tang, J. Guo, Sep. Purif. Technol. 251 (2020) 117357.
[10] Q. Guo, C. Zhou, Z. Ma, X. Yang, Adv. Mater. 31 (2019) e1901997.
[11] M. Cheng, Y. Liu, D. Huang, C. Lai, G. Zeng, J. Huang, Z. Liu, C. Zhang, C. Zhou, L. Qin, W. Xiong, H. Yi, Y. Yang, Chem. Eng. J. 362 (2019) 865–876.
[12] C. Zhou, G. Zeng, D. Huang, Y. Luo, M. Cheng, Y. Liu, W. Xiong, Y. Yang, B. Song, W. Wang, B. Shao, Z. Li, J. Hazard. Mater. 386 (2020) 121947.
[13] S. Ye, M. Yan, X. Tan, J. Liang, G. Zeng, H. Wu, B. Song, C. Zhou, Y. Yang, H. Wang, Appl. Catal. B 250 (2019) 78–88.
[14] H. Yi, M. Yan, D. Huang, G. Zeng, C. Lai, M. Li, X. Huo, L. Qin, S. Liu, X. Liu, B. Li, H. Wang, M. Shen, Y. Fu, X. Guo, Appl. Catal. B 250 (2019) 52–62.
[15] L. Wang, J. Zhao, H. Liu, J. Huang, J. Taiwan Inst. Chem. Eng. 93 (2018) 590–602.
[16] J. Schneider, M. Matsuoka, M. Takeuchi, J. Zhang, Y. Horiuchi, M. Anpo, D.W. Bahnemann, Chem. Rev. 114 (2014) 9919–9986.
[17] K. Maeda, T. Takata, M. Hara, N. Saito, Y. Inoue, H. Kobayashi, K. Domen 127 (2005) 8286–8287.
[18] Y. Xu, W. Zhao, R. Xu, Y. Shi, B. Zhang, Chem. Commun. 49 (2013).
[19] M. Tabata, K. Maeda, T. Ishihara, T. Minegishi, T. Takata, K. Domen, J. Phys. Chem. C 114 (2010) 11215–11220.
[20] W. Wang, Q. Niu, G. Zeng, C. Zhang, D. Huang, B. Shao, C. Zhou, Y. Yang, Y. Liu, H. Guo, W. Xiong, L. Lei, S. Liu, H. Yi, S. Chen, X. Tang, Appl. Catal. B 273 (2020) 119051.
[21] W. Wang, C. Zhou, Y. Yang, G. Zeng, C. Zhang, Y. Zhou, J. Yang, D. Huang, H. Wang, W. Xiong, X. Li, Y. Fu, Z. Wang, Q. He, M. Jia, H. Luo, Chem. Eng. J. 404 (2021) 126540.
[22] J. Qiu, X. Zhang, Y. Feng, X. Zhang, H. Wang, J. Yao, Appl. Catal. B 231 (2018) 317–342.
[23] C. Janiak, J.K. Vieth, New J. Chem. 34 (2010).
[24] G. Zhong, D. Liu, J. Zhang, Cryst. Growth Des. 18 (2018) 7730–7744.
[25] T. Loiseau, C. Serre, C. Huguenard, G. Fink, F. Taulelle, M. Henry, T. Bataille, G. Ferey, Chemistry 10 (2004) 1373–1382.
[26] S. Bhattacharjee, C. Chen, W.-S. Ahn, RSC Adv. 4 (2014) 52500–52525.
[27] H.R. Abid, Z.H. Rada, J. Shang, S. Wang, Polyhedron 120 (2016) 103–111.
[28] Y. Wang, J. Yan, N. Wen, H. Xiong, S. Cai, Q. He, Y. Hu, D. Peng, Z. Liu, Y. Liu, Biomaterials 230 (2020) 119619.
[29] W.T. Xu, L. Ma, F. Ke, F.M. Peng, G.S. Xu, Y.H. Shen, J.F. Zhu, L.G. Qiu, Y.P. Yuan, Dalton Trans. 43 (2014) 3792–3798.
[30] Z. Lionet, T.-H. Kim, Y. Horiuchi, S.W. Lee, M. Matsuoka, J. Phys. Chem. C 123 (2019) 27501–27508.
[31] C. Xu, R. Fang, R. Luque, L. Chen, Y. Li, Coord. Chem. Rev. 388 (2019) 268–292.
[32] M. Cheng, C. Lai, Y. Liu, G. Zeng, D. Huang, C. Zhang, L. Qin, L. Hu, C. Zhou, W. Xiong, Coord. Chem. Rev. 368 (2018) 80–92.
[33] Q. Wang, Q. Gao, A.M. Al-Enizi, A. Nafady, S. Ma, Inorg. Chem. Front. 7 (2020) 300–339.
[34] Y. Fu, H. Yang, R. Du, G. Tu, C. Xu, F. Zhang, M. Fan, W. Zhu, RSC Adv. 7 (2017) 42819–42825.
[35] M. Duan, L. Jiang, G. Zeng, D. Wang, W. Tang, J. Liang, H. Wang, D. He, Z. Liu, L. Tang, Appl. Mater. Today 19 (2020) 100564.
[36] F. Song, W. Li, Y. Sun, Inorganics 5 (2017) 40.
[37] S. Kampouri, T.N. Nguyen, M. Spodaryk, R.G. Palgrave, A. Züttel, B. Smit, K.C. Stylianou, Adv. Funct. Mater. 28 (2018) 1806368.
[38] X. Yang, X. Qi, G. Ma, Z. Li, Q. Liu, S. Khan, Y. Zhao, L. Zhang, Z. Geng, Y. Guo, Appl. Surf. Sci. 479 (2019) 1048–1056.
[39] Y. Fang, Y. Ma, M. Zheng, P. Yang, A.M. Asiri, X. Wang, Coord. Chem. Rev. 373 (2018) 83–115.
[40] X. Liu, Y. Zhou, J. Zhang, L. Tang, L. Luo, G. Zeng, ACS Appl. Mater. Interfaces 9 (2017) 20255–20275.
[41] Y. Shi, A.-F. Yang, C.-S. Cao, B. Zhao, Coord. Chem. Rev. 390 (2019) 50–75.
[42] D. Jiang, P. Xu, H. Wang, G. Zeng, D. Huang, M. Chen, C. Lai, C. Zhang, J. Wan, W. Xue, Coord. Chem. Rev. 376 (2018) 449–466.
[43] Y. Liu, D. Huang, M. Cheng, Z. Liu, C. Lai, C. Zhang, C. Zhou, W. Xiong, L. Qin, B. Shao, Q. Liang, Coord. Chem. Rev. 409 (2020).
[44] K.G. Laurier, F. Vermoortele, R. Ameloot, D.E. De Vos, J. Hofkens, M.B. Roeffaers, J. Am. Chem. Soc. 135 (2013) 14488–14491.
[45] D. Wang, R. Huang, W. Liu, D. Sun, Z. Li, ACS Catal. 4 (2014) 4254–4260.
[46] R. Liang, F. Jing, L. Shen, N. Qin, L. Wu, J. Hazard. Mater. 287 (2015) 364–372.
[47] Y. Gao, G. Yu, K. Liu, S. Deng, B. Wang, J. Huang, Y. Wang, Chem. Eng. J. 330 (2017) 157–165.
[48] B. Xu, H. Yang, Y. Cai, H. Yang, C. Li, Inorg. Chem. Commun. 67 (2016) 29–31.
[49] F. Jing, R. Liang, J. Xiong, R. Chen, S. Zhang, Y. Li, L. Wu, Appl. Catal. B 206 (2017) 9–15.
[50] Y. Liu, H. Cheng, M. Cheng, Z. Liu, D. Huang, G. Zhang, B. Shao, Q. Liang, S. Luo, T. Wu, S. Xiao, Chem. Eng. J. (2020) 127914.
[51] W. Mei, D. Li, H. Xu, J. Zan, L. Sun, Q. Li, B. Zhang, Y. Wang, D. Xia, Chem. Phys. Lett. 706 (2018) 694–701.
[52] C. Gao, S. Chen, X. Quan, H. Yu, Y. Zhang, J. Catal. 356 (2017) 125–132.
[53] H. Hu, H. Zhang, Y. Chen, Y. Chen, L. Zhuang, H. Ou, Chem. Eng. J. 368 (2019) 273–284.
[54] L. Ai, C. Zhang, L. Li, J. Jiang, Appl. Catal. B 148–149 (2014) 191–200.

[55] Y. Gao, S. Li, Y. Li, L. Yao, H. Zhang, Appl. Catal. B 202 (2017) 165–174.
[56] Y. Zhang, J. Zhou, X. Chen, L. Wang, W. Cai, Chem. Eng. J. 369 (2019) 745–757.
[57] J. Castells-Gil, M.P.N.N. Almora-Barrios, I. da Silva, D. Mateo, J. Albero, H. Garcia, C. Marti-Gastaldo, Chem. Sci. 10 (2019) 4313–4321.
[58] M. Dan-Hardi, C. Serre, T.o. Frot, L. Rozes, G. Maurin, C.m. Sanchez, G.r. Férey, J. Am. Chem. Soc. 131 (2009) 10857–10859.
[59] H. Assi, L.C. Pardo Perez, G. Mouchaham, F. Ragon, M. Nasalevich, N. Guillou, C. Martineau, H. Chevreau, F. Kapteijn, J. Gascon, P. Fertey, E. Elkaim, C. Serre, T. Devic, Inorg. Chem. 55 (2016) 7192–7199.
[60] Y. Yan, C. Li, Y. Wu, J. Gao, Q. Zhang, J. Mater. Chem. A 8 (2020) 15245–15270.
[61] P.D. Du, H.T.M. Thanh, T.C. To, H.S. Thang, M.X. Tinh, T.N. Tuyen, T.T. Hoa, D.Q. Khieu, J. Nanomat. 2019 (2019) 1–15.
[62] J.J. Du, Y.P. Yuan, J.X. Sun, F.M. Peng, X. Jiang, L.G. Qiu, A.J. Xie, Y.H. Shen, J.F. Zhu, J. Hazard. Mater. 190 (2011) 945–951.
[63] K. Liu, Y. Gao, J. Liu, Y. Wen, Y. Zhao, K. Zhang, G. Yu, Environ. Sci. Technol. 50 (2016) 3634–3640.
[64] Y. Zhang, F. Mao, L. Wang, H. Yuan, P.F. Liu, H.G. Yang, Solar RRL 4 (2020) 1900438.
[65] L. Jiao, Y. Wang, H.L. Jiang, Q. Xu, Adv. Mater. 30 (2018) e1703663.
[66] Y. Fu, D. Sun, Y. Chen, R. Huang, Z. Ding, X. Fu, Z. Li, Angew. Chem. Int. Ed. Engl. 51 (2012) 3364–3367.
[67] H. Huang, X.-S. Wang, D. Philo, F. Ichihara, H. Song, Y. Li, D. Li, T. Qiu, S. Wang, J. Ye, Appl. Catal. B 267 (2020).
[68] L. Shi, T. Wang, H. Zhang, K. Chang, X. Meng, H. Liu, J. Ye, Adv. Sci. (Weinh) 2 (2015) 1500006.
[69] X.Y. Dao, J.H. Guo, Y.P. Wei, F. Guo, Y. Liu, W.Y. Sun, Inorg. Chem. 58 (2019) 8517–8524.
[70] C.H. Hendon, D. Tiana, M. Fontecave, C. Sanchez, L. D'Arras, C. Sassoye, L. Rozes, C. Mellot-Draznieks, A. Walsh, J. Am. Chem. Soc. 135 (2013) 10942–10945.
[71] M.W. Logan, S. Ayad, J.D. Adamson, T. Dilbeck, K. Hanson, F.J. Uribe-Romo, J. Mater. Chem. A 5 (2017) (1863) 11854–11861.
[72] R. Liang, R. Huang, X. Wang, S. Ying, G. Yan, L. Wu, Appl. Surf. Sci. 464 (2019) 396–403.
[73] S.-Y. Han, D.-L. Pan, H. Chen, X.-B. Bu, Y.-X. Gao, H. Gao, Y. Tian, G.-S. Li, G. Wang, S.-L. Cao, C.-Q. Wan, G.-C. Guo, Angew. Chem. Int. Ed. 57 (2018) 9864–9869.
[74] X. Lian, B. Yan, Inorg. Chem. 55 (2016) (1838) 11831–11841.
[75] X. Chen, S. Xiao, H. Wang, W. Wang, Y. Cai, G. Li, M. Qiao, J. Zhu, H. Li, D. Zhang, Y. Lu, Angew. Chem. Int. Ed. Engl. 59 (2020) 1–6.
[76] F. Zhang, B. Zhang, J. Feng, X. Tan, L. Liu, L. Liu, B. Han, L. Zheng, J. Zhang, J. Tai, J. Zhang, ACS Appl. Energy Mater. 2 (2019) 4964–4970.
[77] S. Wang, F. Meng, X. Sun, M. Bao, J. Ren, S. Yu, Z. Zhang, J. Ke, L. Zeng, Appl. Surf. Sci. 528 (2020) 147053.
[78] M. Wang, L. Yang, C. Guo, X. Liu, L. He, Y. Song, Q. Zhang, X. Qu, H. Zhang, Z. Zhang, S. Fang, Chem. Select 3 (2018) 3664–3674.
[79] N. Tian, Z.-Y. Zhou, S.-G. Sun, Y. Ding, Z.L. Wang, Science 316 (2007) 732–735.
[80] S. Amirjalayer, M. Tafipolsky, R. Schmid, J. Phys. Chem. Lett. 5 (2014) 3206–3210.
[81] S. Ghosh, P. Roy, N. Karmodak, E.D. Jemmis, G. Mugesh, Angew. Chem. Int. Ed. Engl. 57 (2018) 4510–4515.
[82] F. Guo, J.H. Guo, P. Wang, Y.S. Kang, Y. Liu, J. Zhao, W.Y. Sun, Chem. Sci. 10 (2019) 4834–4838.
[83] Y. Ren, M. Shi, W. Zhang, D.D. Dionysiou, J. Lu, C. Shan, Y. Zhang, L. Lv, B. Pan, Environ. Sci. Technol. 54 (2020) 5258–5267.
[84] Y. Horiuchi, T. Toyao, M. Saito, K. Mochizuki, M. Iwata, H. Higashimura, M. Anpo, M. Matsuoka, J. Phys. Chem. C 116 (2012) 20848–20853.
[85] D. Wang, Y. Song, J. Cai, L. Wu, Z. Li, New J. Chem. 40 (2016) 9170–9175.
[86] Y. An, B. Xu, Y. Liu, Z. Wang, P. Wang, Y. Dai, X. Qin, X. Zhang, B. Huang, Chem. Open 6 (2017) 701–705.
[87] R. Liang, S. Luo, F. Jing, L. Shen, N. Qin, L. Wu, Appl. Catal. B 176–177 (2015) 240–248.
[88] R. Liang, F. Jing, L. Shen, N. Qin, L. Wu, Nano Res. 8 (2015) 3237–3249.
[89] D. Wang, Z. Li, J. Catal. 342 (2016) 151–157.
[90] S. Dong, Z. Liu, R. Liu, L. Chen, J. Chen, Y. Xu, ACS Appl. Nano Mater. 1 (2018) 4247–4257.
[91] C. Han, M.-Y. Qi, Z.-R. Tang, J. Gong, Y.-J. Xu, Nano Today 27 (2019) 48–72.
[92] F. Guo, S. Yang, Y. Liu, P. Wang, J. Huang, W.-Y. Sun, ACS Catal. 9 (2019) 8464–8470.
[93] J. Qiu, L. Yang, M. Li, J. Yao, Mater. Res. Bull. 112 (2019) 297–306.
[94] J.D. Xiao, L. Han, J. Luo, S.H. Yu, H.L. Jiang, Angew. Chem. Int. Ed. Engl. 57 (2018) 1103–1107.
[95] M.A. Nasalevich, R. Becker, E.V. Ramos-Fernandez, S. Castellanos, S.L. Veber, M.V. Fedin, F. Kapteijn, J.N.H. Reek, J.I. van der Vlugt, J. Gascon, Energy Environ. Sci. 8 (2015) 364–375.
[96] Z. Li, J.-D. Xiao, H.-L. Jiang, ACS Catal. 6 (2016) 5359–5365.
[97] K. Meyer, S. Bashir, J. Llorca, H. Idriss, M. Ranocchiari, J.A. van Bokhoven, Chemistry 22 (2016) 13894–13899.
[98] R. Wang, L. Wu, B. Chica, L. Gu, G. Xu, Y. Yuan, J. Materiomics 3 (2017) 58–62.
[99] W. Zhen, H. Gao, B. Tian, J. Ma, G. Lu, ACS Appl. Mater. Interfaces 8 (2016) 10808–10819.
[100] D.-Y. Du, J.-S. Qin, S.-L. Li, Z.-M. Su, Y.-Q. Lan, Chem. Soc. Rev. 43 (2014) 4615–4632.
[101] W.A. Shah, A. Waseem, M.A. Nadeem, P. Kögerler, Appl. Catal. A 567 (2018) 132–138.
[102] J. Han, D. Wang, Y. Du, S. Xi, Z. Chen, S. Yin, T. Zhou, R. Xu, Appl. Catal. A 521 (2016) 83–89.
[103] J. Manna, T.P. Vinod, K. Flomin, R. Jelinek, J. Colloid Interface Sci. 460 (2015) 113–118.
[104] J. Low, J. Yu, M. Jaroniec, S. Wageh, A.A. Al-Ghamdi, Adv. Mater. 29 (2017) 1601694.
[105] X. He, V. Nguyen, Z. Jiang, D. Wang, Z. Zhu, W.-N. Wang, Catal. Sci. Technol. 8 (2018) 2117–2123.
[106] S. Kohtani, M. Tomohiro, K. Tokumura, R. Nakagaki, Appl. Catal. B 58 (2005) 265–272.
[107] N. Chang, Y.-X. Li, D.-Y. He, Z.-W. Tang, Y.-F. Huang, J.-J. Yu, Anal. Methods 9 (2017) 381–384.
[108] R. Yuan, C. Yue, J. Qiu, F. Liu, A. Li, Appl. Catal. B 251 (2019) 229–239.
[109] Y. Du, L. Zhao, H. Chen, Z. Huang, X. He, W. Fang, W. Li, F. Zhang, G. Wang, J. Mater. Sci.: Mater. Electron. 29 (2018) 20356–20366.
[110] X. Zhao, Y. Zhang, P. Wen, G. Xu, D. Ma, P. Qiu, Mole. Catal. 452 (2018) 175–183.
[111] X. He, H. Fang, D.J. Gosztola, Z. Jiang, P. Jena, W.N. Wang, ACS Appl. Mater. Interfaces 11 (2019) 12516–12524.
[112] H. Sheng, D. Chen, N. Li, Q. Xu, H. Li, J. He, J. Lu, Chem. Mater. 29 (2017) 5612–5616.
[113] Y. Li, J. Jiang, Y. Fang, Z. Cao, D. Chen, N. Li, Q. Xu, J. Lu, ACS Sustain. Chem. Eng. 6 (2018) 16186–16197.
[114] X. Liu, R. Dang, W. Dong, X. Huang, J. Tang, H. Gao, G. Wang, Appl. Catal. B 209 (2017) 506–513.
[115] H.U. Rasheed, X. Lv, S. Zhang, W. Wei, N. ullah, J. Xie, Adv. Powder Technol. 29 (2018) 3305–3314.
[116] H. Zhao, L. Qian, H. Lv, Y. Wang, G. Zhao, Chem. Cat. Chem. 7 (2015) 4148–4155.
[117] C.-F. Zhang, L.-G. Qiu, F. Ke, Y.-J. Zhu, Y.-P. Yuan, G.-S. Xu, X. Jiang, J. Mater. Chem. A 1 (2013) 14329.
[118] Z. Jin, W. Dong, M. Yang, J. Wang, H. Gao, G. Wang, Chem. Cat. Chem. 8 (2016) 3510–3517.
[119] H. Wang, X. Yuan, Y. Wu, X. Chen, L. Leng, G. Zeng (2015) 32531–32535.
[120] H. Hao, X. Lang, Chem. Cat. Chem. (2018).
[121] J.-Y. Li, Y.-H. Li, M.-Y. Qi, Q. Lin, Z.-R. Tang, Y.-J. Xu, ACS Catal. 10 (2020) 6262–6280.
[122] Y. Liu, S. Shen, J. Zhang, W. Zhong, X. Huang, Appl. Surf. Sci. 478 (2019) 762–769.
[123] F. Ke, L. Wang, J. Zhu, Nano Res. 8 (6) (2015) 1834–1846.
[124] J. Ran, J. Yu, M. Jaroniec, Green Chem. 13 (2011) 2708.
[125] S. Wang, X. Wang, Appl. Catal. B 162 (2015) 494–500.
[126] J.-Y. Yua, Z.-J. Chen, X.-Y. Zeng, C. Liu, F.-Y. Cai, H.-L. Cao, J. Lü, Inorg. Chem. Commun. 95 (2018) 134–138.
[127] R. Wu, S. Wang, Y. Zhou, J. Long, F. Dong, W. Zhang, ACS Appl. Nano Mater. 2 (2019) 6818–6827.
[128] B. Weng, M.-Y. Qi, C. Han, Z.-R. Tang, Y.-J. Xu, ACS Catal. 9 (2019) 4642–4687.
[129] Y. Wang, Y. Zhang, Z. Jiang, G. Jiang, Z. Zhao, Q. Wu, Y. Liu, Q. Xu, A. Duan, C. Xu, Appl. Catal. B 185 (2016) 307–314.
[130] J. Aguilera-Sigalat, D. Bradshaw, Coord. Chem. Rev. 307 (2016) 267–291.
[131] S. Gao, W. Cen, Q. Li, J. Li, Y. Lu, H. Wang, Z. Wu, Appl. Catal. B 227 (2018) 190–197.
[132] R. Yuan, J. Qiu, C. Yue, C. Shen, D. Li, C. Zhu, F. Liu, A. Li, Chem. Eng. J. 401 (2020) 126020.
[133] H. Wang, X. Yuan, Y. Wu, G. Zeng, H. Dong, X. Chen, L. Leng, Z. Wu, L. Peng, Appl. Catal. B 186 (2016) 19–29.
[134] S. Zhang, M. Du, Z. Xing, Z. Li, K. Pan, W. Zhou, Appl. Catal. B 262 (2020) 118202.
[135] D. Wang, B. Su, Y. Jiang, L. Li, B.K. Ng, Z. Wu, F. Liu, Chem. Eng. J. 330 (2017) 102–108.
[136] Y. Yu, G.H. Nam, Q. He, X.J. Wu, K. Zhang, Z. Yang, J. Chen, Q. Ma, M. Zhao, Z. Liu, F.R. Ran, X. Wang, H. Li, X. Huang, B. Li, Q. Xiong, Q. Zhang, Z. Liu, L. Gu, Y. Du, W. Huang, H. Zhang, Nat. Chem. 10 (2018) 638–643.
[137] T.N. Nguyen, S. Kampouri, B. Valizadeh, W. Luo, D. Ongari, O.M. Planes, A. Zuttel, B. Smit, K.C. Stylianou, ACS Appl. Mater. Interfaces 10 (2018) 30035–30039.
[138] N. Liu, W. Huang, M. Tang, C. Yin, B. Gao, Z. Li, L. Tang, J. Lei, L. Cui, X. Zhang, Chem. Eng. J. 359 (2019) 254–264.
[139] S.R. Zhu, P.F. Liu, M.K. Wu, W.N. Zhao, G.C. Li, K. Tao, F.Y. Yi, L. Han, Dalton Trans. 45 (2016) 17521–17529.
[140] M. Jahurul Islam, H.K. Kim, D. Amaranatha Reddy, Y. Kim, R. Ma, H. Baek, J. Kim, T.K. Kim, Dalton Trans. 46 (2017) 6013–6023.
[141] Q. Hu, J. Di, B. Wang, M. Ji, Y. Chen, J. Xia, H. Li, Y. Zhao, Appl. Surf. Sci. 466 (2019) 525–534.
[142] S.G. Khasevani, M.R. Gholami, Ind. Eng. Chem. Res. 58 (2019) 9806–9818.
[143] R.M. Abdelhameed, D.M. Tobaldi, M. Karmaoui, J. Photochem. Photobiol., A 351 (2018) 50–58.
[144] H.E. Emam, H.B. Ahmed, E. Gomaa, M.H. Helal, R.M. Abdelhameed, J. Photochem. Photobiol., A 383 (2019) 111986.
[145] Z. Yang, X. Xu, X. Liang, C. Lei, Y. Wei, P. He, B. Lv, H. Ma, Z. Lei, Appl. Catal. B 198 (2016) 112–123.
[146] N. Zhang, M.Q. Yang, S. Liu, Y. Sun, Y.J. Xu, Chem. Rev. 115 (2015) 10307–10377.
[147] C. Yang, X. You, J. Cheng, H. Zheng, Y. Chen, Appl. Catal. B 200 (2017) 673–680.
[148] C. Zhang, L. Ai, J. Jiang, Ind. Eng. Chem. Res. 54 (2014) 153–163.

[149] R. Liang, L. Shen, F. Jing, N. Qin, L. Wu, ACS Appl. Mater. Interfaces 7 (2015) 9507–9515.
[150] C. Petit, T.J. Bandosz, Adv. Funct. Mater. 21 (2011) 2108–2117.
[151] E. Elsayed, H. Wang, P.A. Anderson, R. Al-Dadah, S. Mahmoud, H. Navarro, Y. Ding, J. Bowen, Microporous Mesoporous Mater. 244 (2017) 180–191.
[152] J. Lin, H. Hu, N. Gao, J. Ye, Y. Chen, H. Ou, J. Water Process Eng. 33 (2020) 101010.
[153] M. Muschi, C. Serre, Coord. Chem. Rev. 387 (2019) 262–272.
[154] Y. Wu, H. Luo, H. Wang, RSC Adv. 4 (2014) 40435–40438.
[155] Y. Yang, W. Wang, H. Li, X. Jin, H. Wang, L. Zhang, Y. Zhang, Mater. Lett. 197 (2017) 17–20.
[156] Z. Wang, H. Wang, Z. Zeng, G. Zeng, P. Xu, R. Xiao, D. Huang, X. Chen, L. He, C. Zhou, Y. Yang, Z. Wang, W. Wang, W. Xiong, Appl. Catal. B 267 (2020) 118700.
[157] Y. Yang, C. Zhang, D. Huang, G. Zeng, J. Huang, C. Lai, C. Zhou, W. Wang, H. Guo, W. Xue, R. Deng, M. Cheng, W. Xiong, Appl. Catal. B 245 (2019) 87–99.
[158] W. Wang, Z. Zeng, G. Zeng, C. Zhang, R. Xiao, C. Zhou, W. Xiong, Y. Yang, L. Lei, Y. Liu, D. Huang, M. Cheng, Y. Yang, Y. Fu, H. Luo, Y. Zhou, Chem. Eng. J. 378 (2019) 122132.
[159] Y. Yang, Z. Zeng, G. Zeng, D. Huang, R. Xiao, C. Zhang, C. Zhou, W. Xiong, W. Wang, M. Cheng, W. Xue, H. Guo, X. Tang, D. He, Appl. Catal. B 258 (2019) 117956.
[160] B. Song, Z. Zeng, G. Zeng, J. Gong, R. Xiao, S. Ye, M. Chen, C. Lai, P. Xu, X. Tang, Adv. Colloid Interface Sci. 272 (2019) 101999.
[161] G. Zhang, D. Huang, M. Cheng, L. Lei, S. Chen, R. Wang, W. Xue, Y. Liu, Y. Chen, Z. Li, J. Mater. Chem. A 8 (2020) 17883–17906.
[162] H. Wang, X. Yuan, Y. Wu, G. Zeng, X. Chen, L. Leng, H. Li, Appl. Catal. B 174–175 (2015) 445–454.
[163] Y. Gong, B. Yang, H. Zhang, X. Zhao, J. Mater. Chem. A 6 (2018) 23703–23711.
[164] X.-Y. Dao, X.-F. Xie, J.-H. Guo, X.-Y. Zhang, Y.-S. Kang, W.-Y. Sun, ACS Appl. Energy Mater. 3 (2020) 3946–3954.
[165] C. Bai, J. Bi, J. Wu, H. Meng, Y. Xu, Y. Han, X. Zhang, Appl. Organomet. Chem. 32 (2018) e4597.
[166] J. Huang, X. Zhang, H. Song, C. Chen, F. Han, C. Wen, Appl. Surf. Sci. 441 (2018) 85–98.
[167] Z. Su, B. Zhang, J. Shi, D. Tan, F. Zhang, L. Liu, X. Tan, D. Shao, G. Yang, J. Zhang, Sustain. Energy Fuels 3 (2019) 1233–1238.
[168] J. Xu, J. Gao, C. Wang, Y. Yang, L. Wang, Appl. Catal. B 219 (2017) 101–108.
[169] Y. Li, Y. Fang, Z. Cao, N. Li, D. Chen, Q. Xu, J. Lu, Appl. Catal. B 250 (2019) 150–162.
[170] G. Zhou, M.-F. Wu, Q.-J. Xing, F. Li, H. Liu, X.-B. Luo, J.-P. Zou, J.-M. Luo, A.-Q. Zhang, Appl. Catal. B 220 (2018) 607–614.
[171] Z. Shao, D. Zhang, H. Li, C. Su, X. Pu, Y. Geng, Sep. Purif. Technol. 220 (2019) 16–24.
[172] Y.-L. Men, P. Liu, X. Peng, Y.-X. Pan, Sci. China Chem. 63 (2020) 1416–1427.
[173] L. Shao, Z. Yu, X. Li, X. Li, H. Zeng, X. Feng, Appl. Surf. Sci. 505 (2020) 144616.
[174] D. Yan, H. Hu, N. Gao, J. Ye, H. Ou, Appl. Surf. Sci. 498 (2019) 143836.
[175] Q. Wang, G. Wang, X. Liang, X. Dong, X. Zhang, Appl. Surf. Sci. 467–468 (2019) 320–327.
[176] M.-J. Chang, W.-N. Cui, X.-J. Chai, J. Liu, K. Wang, L. Qiu, J. Mater. Sci.: Mater. Electron. 30 (2018) 1009–1016.
[177] Y.-Z. Chen, R. Zhang, L. Jiao, H.-L. Jiang, Coord. Chem. Rev. 362 (2018) 1–23.
[178] W. Zhan, L. Sun, X. Han, Nanomicro Lett 11 (2019) 1.
[179] Z. Liu, Y. Wu, J. Chen, Y. Li, J. Zhao, K. Gao, P. Na, Catal. Sci. Technol. 8 (2018) 1936–1944.
[180] J. Li, X. Xu, X. Liu, W. Qin, M. Wang, L. Pan, J. Alloy. Compd. 690 (2017) 640–646.
[181] J. Li, X. Xu, X. Liu, W. Qin, L. Pan, Ceram. Int. 43 (2017) 835–840.
[182] B. Liu, L. Peng, J. Alloy. Compd. 571 (2013) 145–152.
[183] L. Jing, W. Zhou, G. Tian, H. Fu, Chem. Soc. Rev. 42 (2013) 9509–9549.
[184] Z. Guo, J.K. Cheng, Z. Hu, M. Zhang, Q. Xu, Z. Kang, D. Zhao, RSC Adv. 4 (2014) 34221–34225.
[185] H. Liu, Y. Ma, J. Chen, M. Wen, G. Li, T. An, Appl. Catal. B 250 (2019) 337–346.
[186] K. Khaletskaya, A. Pougin, R. Medishetty, C. Rösler, C. Wiktor, J. Strunk, R.A. Fischer, Chem. Mater. 27 (2015) 7248–7257.
[187] B. Yan, L. Zhang, Z. Tang, M. Al-Mamun, H. Zhao, X. Su, Appl. Catal. B 218 (2017) 743–750.
[188] N. Li, B. Wang, Y. Si, F. Xue, J. Zhou, Y. Lu, M. Liu, ACS Catal. 9 (2019) 5590–5602.
[189] F. Wang, X. He, L. Sun, J. Chen, X. Wang, J. Xu, X. Han, J. Mater. Chem. A 6 (2018) 2091–2099.
[190] N.W. Othman, H. Radde, P.Y. Puah, Y.S. Ling, P.Y. Moh, J. Chin. Chem. Soc. 66 (2019) 81–88.
[191] K.E. deKrafft, C. Wang, W. Lin, Adv. Mater. 24 (2012) 2014–2018.
[192] M.H. Pham, C.T. Dinh, G.T. Vuong, N.D. Ta, T.O. Do, PCCP 16 (2014) 5937–5941.
[193] H. Zhang, T. Wang, J. Wang, H. Liu, T.D. Dao, M. Li, G. Liu, X. Meng, K. Chang, L. Shi, T. Nagao, J. Ye, Adv. Mater. 28 (2016) 3703–3710.
[194] J.D. Xiao, H.L. Jiang, Small 13 (2017) 1700632.
[195] H. Xiao, W. Zhang, Q. Yao, L. Huang, L. Chen, B. Boury, Z. Chen, Appl. Catal. B 244 (2019) 719–731.
[196] Y. Fang, S.-R. Zhu, M.-K. Wu, W.-N. Zhao, L. Han, J. Solid State Chem. 266 (2018) 205–209.
[197] S. Wang, B.Y. Guan, Y. Lu, X.W.D. Lou, J. Am. Chem. Soc. 139 (2017) 17305–17308.